Mechanical Systems and Signal Processing 165 (2022) 108388

Contents lists available at ScienceDirect

Mechanical Systems and Signal Processing

journal homepage: www.elsevier.com/locate/ymssp

Local resonator stimulated polarization transition in metamaterials and the formation of topological interface states

Guobiao Hu [a], Chunbo Lan [b], Lihua Tang [c], Yaowen Yang [a,*]

[a] School of Civil and Environmental Engineering, Nanyang Technological University, 50 Nanyang Avenue, 639798 Singapore, Singapore
[b] College of Aerospace Engineering, Nanjing University of Aeronautics and Astronautics, Nanjing, Jiangsu 210016, China
[c] Department of Mechanical Engineering, University of Auckland, 20 Symonds Street, Auckland 1010, New Zealand

ARTICLE INFO

Keywords:
Topological metamaterial
Polarization transition
Interface state
Zak phase

ABSTRACT

Developing the acoustic-elastic analogy of a topological insulator has attracted extensive research attention in recent years. Designs developed in the literature strongly rely on reforming the host structure of a system to achieve topology transition. In this article, an innovative topological metamaterial is presented. Unlike topological phononic crystals, the proposed topological metamaterial has a uniform host structure without any phononic crystal features. The band inversion and polarization transition are achieved by manipulating the design of local resonators. It has been proven that by changing the coupling spring constant of local resonators, the mode topologies at the bound states associated with the band gaps can be converted. Three polarization transition points have been found from the bound evolution analysis, and all of them possess the capability of stimulating topological interface states in the corresponding band gaps. The Zak phase calculations have further ascertained the prediction about the topological interface states. The band structure and transmittance spectrum of a supercell lattice of the proposed topological metamaterial have been examined. The topological interface states, as well as the energy localization effects, have been successfully observed in all the three band gaps. The proposed metamaterial brings the convenience of creating topological interface states by carefully manipulating the local resonators only. The methodology presented in this work is thus of practical significance in transforming existing structures into topological systems without revising them.

1. Introduction

Over the past two decades, phononic crystals (PCs) and metamaterials have attracted numerous interests due to their unique dynamic properties originated from artificially engineered microstructures [1–6]. In recent years, the research of PCs and metamaterials has been extended to the development of their analogues of topological concepts in condensed matter physics, such as the quantum spin Hall effect [7–10] and topological phases [11–13]. Novel properties and phenomena have been found in topological PCs/metamaterials, including topological interface states [14–20], topological protection [21,22], and energy localization effect [23,24].

Band inversion and polarization transition are believed to be the indications of the occurrence of topological interface states [15,16,25]. Topological invariants like the Zak phase [16,26,27] and the Berry phase [28,29] can be utilized to examine whether band

* Corresponding author.
E-mail address: cywyang@ntu.edu.sg (Y. Yang).

https://doi.org/10.1016/j.ymssp.2021.108388
Received 4 April 2021; Received in revised form 5 July 2021; Accepted 21 August 2021
Available online 1 September 2021

inversion and polarization transition can take place. Modification of the geometric topology has been widely adopted as an effective means to achieve mode polarization transition, since the structural geometry of a mechanical system directly influences its dynamic mode behaviour. To this end, Yin *et al.* [14] developed a one-dimensional (1D) topological PC by designing appropriate thickness variation along the beam. The geometric change altered the mode polarization behaviour, resulting in the generation of the topological interface modes. Based on a similar idea, Muhammad *et al.* [21] extended the work by Yin *et al.* [14] to investigate a topological PC that was consisted of circular beams with piecewise varying cross-sections. By changing geometric parameters, multiple topological interface states could appear in the band gaps. The topological PC proposed by Muhammad *et al.* [21] is an analogue of the acoustic topological system studied by Xiao *et al.* [15]. In fact, instead of varying the geometric shapes, using different materials to construct the host structure can also form a topological PC [27]. The above research focused on the development of topological PCs since the topological interface states were believed to exist only in the Bragg Scattering band gaps [16]. Zhao *et al.* [16] attached local resonators onto a diatomic PC mass-spring chain to form a locally resonant topological metamaterial. It was found that due to the introduction of local resonators, a folding point induced Bragg Scattering band gap was produced in the low-frequency range below the locally resonant band gap. Hence, subwavelength topological interface states appeared in the proposed metamaterial. A more recent study established a locally resonant 1D topological metamaterial beam based on the idea presented in [17]. Similarly, through an artificial enlargement of the unit cell boundary, folded branches formed a resonance-based Dirac cone below the Bragg limit in a two-dimensional spiral-based phononic plate proposed by Foehr *et al.* [30]. By breaking the translational symmetry, a topologically protected band gap was opened at the Dirac cone. The topological interface state was produced by jointing two spiral-based phononic plates with different topologies.

According to the literature review, it can be found that topological interface states have been widely reported in PCs or locally resonant metamaterials with the host structure possessing the PC feature. In such studies, the underlying mechanism for producing topological interface states lies in manipulating the host structure to yield desired change in geometric topology. Though topological metamaterials contain local resonators, the polarization transition is still realized through the PC feature of the host structure [16]. The existence of local resonators only contributes to the formation of folding points as well as the folding points induced subwavelength Bragg Scattering band gaps [16,17,30]. In other words, the formation of topological interface states does not rely on the local resonators. Therefore, two questions naturally arise: (1) Is changing the geometric topology the only means to obtain a topological metamaterial? and (2) Can we manipulate the local resonators instead of the host structure to attain polarization transition and topological interface states?

In this article, an innovative topological metamaterial is proposed and analysed to answer the above questions. The host structure of the proposed topological metamaterial does not have to possess any PC feature, i.e., it can be designed in a uniform manner. It is interestingly found that by just manipulating the design of local resonators, band inversion, polarization transition, and topological interface states can be obtained in the topological metamaterial as well.

The rest of the paper is organized as follows. In Section 2, a previous topological metamaterial model in the literature [16] is reviewed. Section 3 introduces the proposed topological metamaterial and its modelling. In Section 4, conditions for band inversion and polarization transition of the proposed metamaterial are explored. Zak phases are calculated as the criterion to ascertain the existence of topological interface states in the band gaps. In Section 5, the proposed topological metamaterial is constructed by following the derived conditions from Section 4. The topological interface states are confirmed in the band structure and transmittance spectrum analyses of the supercell lattices of the proposed topological metamaterials. Energy localization effects at interface states are illustrated through displacement distribution plots. Conclusions of the present work are summarized in the last section.

2. Review of a previous model

Fig. 1 shows the diatomic metamaterial model studied in [16]. Due to impedance mismatch induced by $K_1 \neq K_2$, the host structure (i.e., outer mass chain) possesses the phononic crystal (PC) feature. Hence, two Bragg Scattering band gaps can be produced in this diatomic chain. On the other hand, one locally resonant band gap is originated from the existence of the local resonators. For this diatomic chain, $K_1 \neq K_2$, or in other words, the impedance mismatch in the host structure is the essential condition to open the two band folding points to form two Bragg Scattering band gaps. Under the condition of $K_1 \neq K_2$, Zhao *et al.* [16] have proved that if a topological metamaterial is constructed by assembling two diatomic chains with swapped K_1 and K_2 on the left and right-hand sides, topological interface states will appear in the two specific Bragg Scattering band gaps. According to their analysis, the second band gap, i.e., the locally resonant band gap, does not support the formation of the interface state.

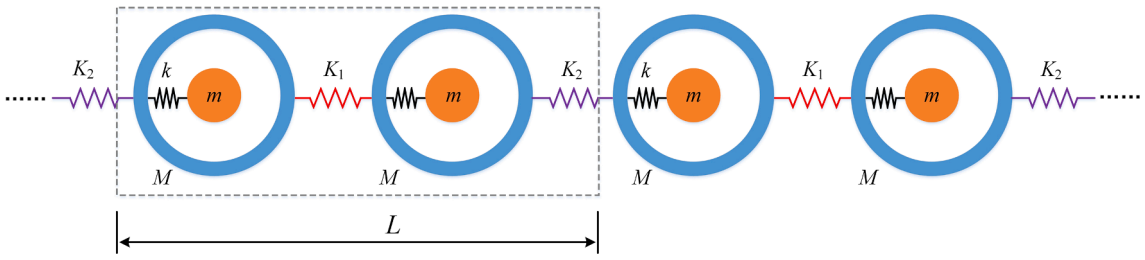

Fig. 1. Schematics of a mass-spring model represented metamaterial consisting of a diatomic chain that has been studied in [16].

Based on their study, we can briefly conclude that if $K_1 = K_2$, the two band folding points will be closed and there will be no Bragg Scattering band gaps. In this way, the diatomic chain cannot be regarded as a topological metamaterial, and interface states will never take place. The research works presented in [14–17,21] lead to the similar conclusion. It is worth emphasizing that regardless of the tuning of the local resonators, the above statement is always valid as long as $K_1 = K_2$. In other words, the existence of the local resonators does not affect the formation of topological interface state at all. Besides, even if $K_1 \neq K_2$, interface states can never be formed in the second band gap of the topological metamaterial. The role of the local resonators is to lower down the frequencies of the band folding points, thus the generated Bragg Scattering band gaps. The consequent advantage is that the interface states could be formed at subwavelength region. In the following sections, a similar but different diatomic chain model will be investigated. It will be demonstrated that unlike previous studies, the design of local resonators plays a dominant role in affecting the formation of topological interface state. Moreover, even if the host structure does not possess the PC feature, i.e., $K_1 = K_2$, topological interface states could still appear.

3. Overview of the present model

In this section, an internally coupled metamaterial shown in Fig. 2 is proposed. The criteria for the occurrence of topological interface states will be derived. As this work is inspired by [16], in which $K_1 \neq K_2$ is an essential condition for producing the topological interface state, we first adopt the same assumption that K_1 could be different from K_2 at the system modelling stage. We will later show that even letting $K_1 = K_2$, interface states can still be stimulated in all the three band gaps of our proposed topological metamaterial.

The governing equations of the internally coupled metamaterial presented in Fig. 2 can be obtained as below.

$$\begin{cases} M\dfrac{d^2u_i}{dt^2} + K_1(u_i - u_j) + K_2(u_i - u_{j-1}) + k(u_i - v_i) = 0 \\ m\dfrac{d^2v_i}{dt^2} + k(v_i - u_i) + K(v_i - v_j) = 0 \\ M\dfrac{d^2u_j}{dt^2} + K_1(u_j - u_i) + K_2(u_j - u_{i+1}) + k(u_j - v_j) = 0 \\ m\dfrac{d^2v_j}{dt^2} + k(v_j - u_j) + K(v_j - v_i) = 0 \end{cases} \tag{1}$$

where M and m denote the outer and the inner masses, respectively. K_1 and K_2 stand for the stiffness constants of the left and right springs that constitute the host structure (i.e., outer mass-spring chain) in each unit cell. k is the spring stiffness of the inside local resonator. u_i and u_j are the displacements of the left and right outer masses in a unit cell. v_i and v_j are the displacements of the left and right inner masses, respectively. To generalize the following analysis, we first introduce the following dimensionless parameters:

$$\begin{cases} \mu = \dfrac{m}{M} \quad \alpha_1 = \dfrac{K_1}{k} \quad \alpha_2 = \dfrac{K_2}{k} \quad \beta = \dfrac{K}{k} \quad \Omega_r = \dfrac{\omega}{\omega_r} \\ \widetilde{u}_i = \dfrac{u_i}{L} \quad \widetilde{u}_j = \dfrac{u_j}{L} \quad \widetilde{v}_i = \dfrac{v_i}{L} \quad \widetilde{v}_j = \dfrac{v_j}{L} \end{cases} \tag{2}$$

where $\omega_r = \sqrt{k/m}$ is the natural frequency of the local resonator. Eq. (1) can then be rewritten in the dimensionless form as:

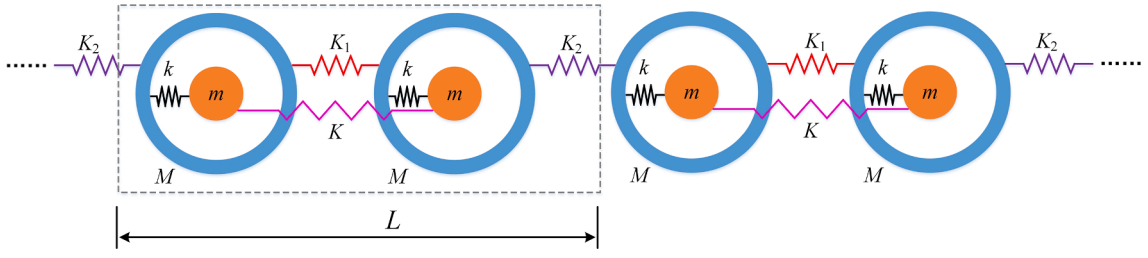

Fig. 2. Schematic of the proposed mass-spring model represented metamaterial consisting of a similar diatomic chain, but with coupling springs connecting local resonators in neighbouring unit cells alternately.

$$\begin{cases} -\frac{1}{\mu}\Omega_r^2 U_i + \alpha_1\left(U_i - U_j\right) + \alpha_2\left(U_i - U_{j-1}\right) + \left(U_i - V_i\right) = 0 \\ -\Omega_r^2 V_i + \left(V_i - U_i\right) + \beta\left(V_i - V_j\right) = 0 \\ -\frac{1}{\mu}\Omega_r^2 U_j + \alpha_1\left(U_j - U_i\right) + \alpha_2\left(U_j - U_{i+1}\right) + \left(U_j - V_j\right) = 0 \\ -\Omega_r^2 V_j + \left(V_j - U_j\right) + \beta\left(V_j - V_i\right) = 0 \end{cases} \tag{3}$$

where the capital U_i, U_j, V_i and V_j are the amplitudes of $\widetilde{u}_i$, $\widetilde{u}_j$, $\widetilde{v}_i$, and $\widetilde{v}_j$, respectively. Applying the Bloch's theorem, the solutions to the mass displacement amplitudes can be assumed in the form as:

$$\begin{cases} U_i = Ae^{Iqx} \\ U_j = Be^{Iqx} \\ V_i = Ce^{Iqx} \\ V_j = De^{Iqx} \end{cases} \tag{4}$$

where I stands for the imaginary number $\sqrt{-1}$. Substituting Eq. (4) into Eq. (3) and rearranging it in the matrix form yields:

$$\begin{bmatrix} 1+\alpha_1+\alpha_2-\frac{\Omega_r^2}{\mu} & -\alpha_1-\alpha_2 e^{Iq} & -1 & 0 \\ -1 & 0 & 1+\beta-\Omega_r^2 & -\beta \\ -\alpha_1-\alpha_2 e^{Iq} & 1+\alpha_1+\alpha_2-\frac{\Omega_r^2}{\mu} & 0 & -1 \\ 0 & -1 & -\beta & 1+\beta-\Omega_r^2 \end{bmatrix} \begin{bmatrix} A \\ B \\ C \\ D \end{bmatrix} = 0 \tag{5}$$

Forcing the determinant of the coefficient matrix of Eq. (5) to be zero to guarantee the existence of nontrivial solutions, the dispersion relation of the internally coupled metamaterial can be derived:

$$\Omega_r^8 + C_6\Omega_r^6 + C_4\Omega_r^4 + C_2\Omega_r^2 + C_0 = 0 \tag{6}$$

The expressions of the polynomial coefficients can be found in the appendix.

4. Band inversion and polarization transition

In the following sections, we let $\alpha_1 = \alpha_2 = \alpha$. It is worth noting that this assumption is not for the sake of simplifying the problem; it indicates that the host structure, i.e., outer mass-spring chain of the metamaterial, keeps consistency without the phononic crystal (PC) feature. Numerous literatures have reported the formation of topological interface states in PCs or metamaterials with host structures possessing the PC feature [12,14–17,21]. In those existing studies, the band inversion was achieved by changing the geometric topology of the host structure. In other words, the mode polarization transition was stimulated by converting the PC feature. A diatomic

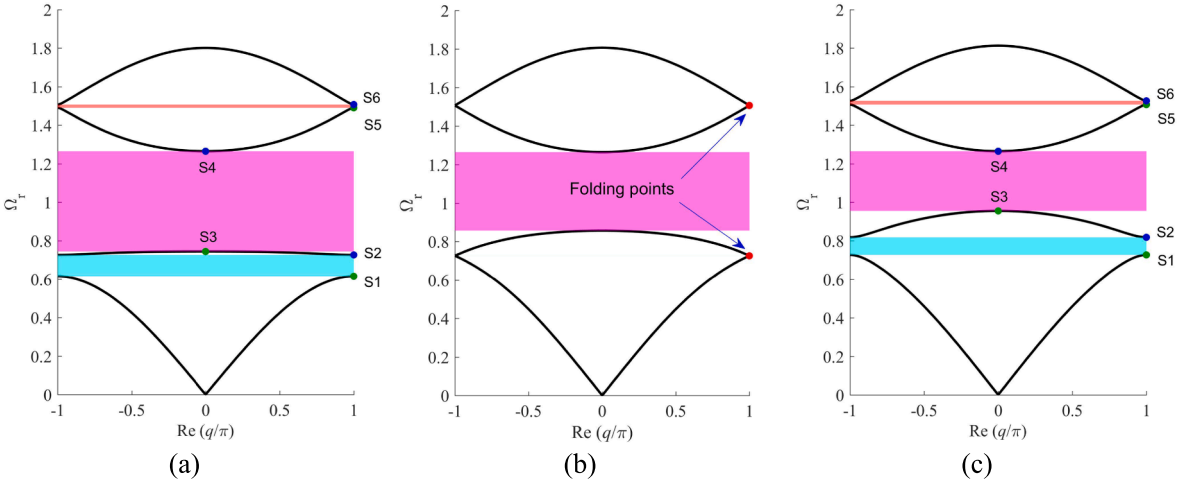

Fig. 3. Band structures of the internally coupled metamaterial with the same $\mu = 0.6$, $\alpha_1 = \alpha_2 = \alpha = 1$, but different dimensionless coupling strength: (a) $\beta = -0.1$, (b) $\beta = 0$, (c) $\beta = 0.1$. The cyan, magenta, and red strips represent the band gaps. q is the dimensionless wavenumber. Re is the operator to extract the real part of the complex number.

metamaterial model presented in [16] with $\alpha_1 = \alpha_2 = \alpha$ can never produce a topological interface state. In the internally coupled metamaterial, it will be proven that by manipulating the local resonators, the topological interface state can still take place even if the host structure is uniform without the PC feature. This interesting phenomenon is one of the novel contributions from the present work.

4.1. Band inversion

According to the dispersion relation depicted by Eq. (6), the band structures of the internally coupled metamaterial (Fig. 2), with β = -0.1, 0, and 0.1 are plotted in Fig. 3.(a), (b), and (c), respectively. Note that other system parameters are kept the same: $\mu = 0.6$, $\alpha_1 = \alpha_2 = \alpha = 1$ for those three cases. Note $\beta = 0$ implies that the internally coupled metamaterial degenerates to the ordinary diatomic model without internal couplings, as shown in Fig. 1. It is noted from Fig. 3.(b) that there is only a single locally resonant band gap (LRBG) in the degenerated diatomic model. Two folding points that are regarded as topological phase-transition points appear separately above and below the LRBG [16]. When $\beta \neq 0$, i.e., in the internally coupled metamaterial, band gaps are opened at the two folding points as shown in Fig. 3.(a) and (c), where S1 to S6 denote the six bound points of the three band gaps.

By solving Eq. (6) and seeking the solutions at $q = 0$ and π, the explicit expressions of the six bounds associated with the three band gaps can be obtained:

$$\begin{cases} f_{\mathrm{I}} = \sqrt{\alpha\mu + \beta + \dfrac{\mu+1}{2} - \dfrac{1}{2}\sqrt{(2\alpha+1)^2\mu^2 + ((-8\beta-4)\alpha - 4\beta + 2)\mu + (2\beta+1)^2}} \\ f_{\mathrm{II}} = \sqrt{2\alpha\mu + \beta + \dfrac{\mu+1}{2} - \dfrac{1}{2}\sqrt{(4\alpha+1)^2\mu^2 + (-8(2\beta+1)\alpha - 4\beta + 2)\mu + (2\beta+1)^2}} \\ f_{\mathrm{III}} = \sqrt{\alpha\mu + \dfrac{\mu+1}{2} - \dfrac{1}{2}\sqrt{(2\alpha+1)^2\mu^2 + (-4\alpha+2)\mu + 1}} \\ f_{\mathrm{IV}} = \sqrt{1+\mu} \\ f_{\mathrm{V}} = \sqrt{\alpha\mu + \beta + \dfrac{\mu+1}{2} + \dfrac{1}{2}\sqrt{(2\alpha+1)^2\mu^2 + ((-8\beta-4)\alpha - 4\beta + 2)\mu + (2\beta+1)^2}} \\ f_{\mathrm{VI}} = \sqrt{\alpha\mu + \dfrac{\mu+1}{2} + \dfrac{1}{2}\sqrt{(2\alpha+1)^2\mu^2 + (-4\alpha+2)\mu + 1}} \end{cases} \tag{7}$$

For varying β, Fig. 4 shows the bound evolution calculated using Eq. (7). The six curves in Fig. 4 are referred to as Bounds I ~ VI, respectively. The formulas in Eq. (7) actually denote the eigen-frequencies for the states at the six bounds of the three band gaps. From the theory of linear algebra, each eigenvalue is paired with a corresponding eigenvector, which contains the modal information of a dynamic system. Therefore, it could be deduced that the state modes related to each curve have a similar form that can be represented by the same eigenvector formula in mathematics.

A transition point is an intersection point of two curves in the bound evolution graph where the band gap vanishes then reopens when leaving this point. Three transition points are observed in Fig. 4. Two of them correspond to the aforementioned two folding points, as shown in Fig. 3.(b). From another point of view, the bounds are inverted while crossing the transition point (i.e., band inversion). In other words, the upper bound goes downward while the lower bound goes upward when passing through the transition point from the left to the right-hand side.

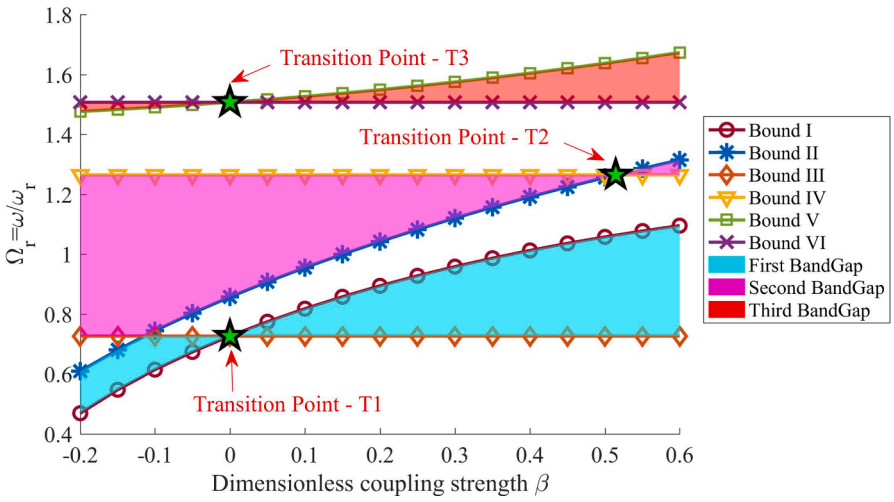

Fig. 4. Bound evolution for varying β. Bounds I ~ VI represent the six bounds of the three band gaps.

4.2. Polarization transition

As mentioned above that each bound curve corresponds to a specific type of mode, the topologies of the modes are converted when the transition takes place. The mode evolutions in the two band gaps that are produced at the left and right of a transition point are supposed to be two opposite processes. Therefore, when the two band gaps of two metamaterials (each of them locates at the left and right of a transition point) lap over, at a certain frequency in the overlapped band gap, the mode topology, i.e., polarization direction, would be inversed, leading to the occurrence of the topological interface state. The band inversion is a necessary condition for polarization transition. The following study explores further proofs of the polarization transitions in the internally coupled metamaterial, thus the formation of topological interface states.

Omitting the time-harmonic factor that applies to all the field variables and applying the Bloch's theorem (i.e., $\widetilde{u}_{i+1} = e^{Iq}\widetilde{u}_i$, $\widetilde{u}_{j-1} = e^{-Iq}\widetilde{u}_j$), Eq. (1) can be transformed into the dimensionless form as:

$$\begin{cases} \left(2\alpha + 1 - \dfrac{\Omega_r^2}{\mu}\right)\widetilde{u}_i - \left(\alpha + \alpha e^{-Iq}\right)\widetilde{u}_j - \widetilde{v}_i = 0 \\ \left(\beta + 1 - \Omega_r^2\right)\widetilde{v}_i - \beta\widetilde{v}_j - \widetilde{u}_i = 0 \\ \left(2\alpha + 1 - \dfrac{\Omega_r^2}{\mu}\right)\widetilde{u}_j - \left(\alpha + \alpha e^{Iq}\right)\widetilde{u}_i - \widetilde{v}_j = 0 \\ \left(\beta + 1 - \Omega_r^2\right)\widetilde{v}_j - \beta\widetilde{v}_i - \widetilde{u}_j = 0 \end{cases} \tag{8}$$

Solving the second and fourth equations of Eq. (8) simultaneously, $\widetilde{v}_i$ and $\widetilde{v}_j$ can be expressed using $\widetilde{u}_i$ and $\widetilde{u}_j$ to reduce the number of unknown variables.

$$\begin{cases} \widetilde{v}_i = a\widetilde{u}_i + b\widetilde{u}_j \\ \widetilde{v}_j = b\widetilde{u}_i + a\widetilde{u}_j \end{cases} \tag{9}$$

where

$$\begin{cases} a = \dfrac{\left(\beta + 1 - \Omega_r^2\right)}{\left[\left(\beta + 1 - \Omega_r^2\right)^2 - \beta^2\right]} \\ b = \dfrac{\beta}{\left[\left(\beta + 1 - \Omega_r^2\right)^2 - \beta^2\right]} \end{cases}$$

Substituting Eq. (9) into the rest two equations of Eq. (8) and writing them in the matrix form,

$$\begin{bmatrix} 0 & \left(\alpha + \alpha e^{-Iq} + b\right) \\ \left(\alpha + \alpha e^{Iq} + b\right) & 0 \end{bmatrix} \begin{pmatrix} \widetilde{u}_i \\ \widetilde{u}_j \end{pmatrix} = \left[2\alpha + (1 - a) - \frac{\Omega_r^2}{\mu}\right] \begin{pmatrix} \widetilde{u}_i \\ \widetilde{u}_j \end{pmatrix} \tag{10}$$

an eigenvalue problem for the internally coupled metamaterial is obtained. The eigenvalue of Eq. (10) can be found to be:

$$\begin{aligned} \lambda(\Omega_r) &= 2\alpha + (1 - a) - \frac{\Omega_r^2}{\mu} = \pm\left|\alpha + \alpha e^{-Iq} + b\right| \\ &= \pm\left|\alpha + \alpha e^{-Iq} + \frac{\beta}{\left[\left(\beta + 1 - \Omega_r^2\right)^2 - \beta^2\right]}\right| \end{aligned} \tag{11}$$

The sign of the eigenvalue and its corresponding eigenvector are dependent on the sign of $2\alpha + (1 - a) - \Omega_r^2/\mu$. Substituting Eq. (7) into Eq. (11), the dimensionless eigenvalue λ could be explicitly written as:

$$\begin{cases} \lambda_1 = 2\alpha+1-\dfrac{2(3+4\beta+2\alpha\mu+\mu-\Gamma_1)}{(3+4\beta+2\alpha\mu+\mu-\Gamma_1)^2-4\beta^2}-\dfrac{(2\alpha+1)\mu+2\beta+1-\Gamma_1}{2\mu} \\ \lambda_2 = 2\alpha+1-\dfrac{2(3+4\beta+4\alpha\mu+\mu-\Gamma_2)}{(3+4\beta+4\alpha\mu+\mu-\Gamma_2)^2-4\beta^2}-\dfrac{(4\alpha+1)\mu+2\beta+1-\Gamma_2}{2\mu} \\ \lambda_3 = 2\alpha+1-\dfrac{2(3+2\beta+2\alpha\mu+\mu-\Gamma_3)}{(3+2\beta+2\alpha\mu+\mu-\Gamma_3)^2-4\beta^2}-\dfrac{(2\alpha+1)\mu+1-\Gamma_3}{2\mu} \\ \lambda_4 = 2\alpha+1-\dfrac{2+\beta+\mu}{(\mu+2)(\mu+2\beta+2)}-\dfrac{1+\mu}{\mu} \\ \lambda_5 = 2\alpha+1-\dfrac{2(3+4\beta+2\alpha\mu+\mu+\Gamma_1)}{(3+4\beta+2\alpha\mu+\mu+\Gamma_1)^2-4\beta^2}-\dfrac{(2\alpha+1)\mu+2\beta+1+\Gamma_1}{2\mu} \\ \lambda_6 = 2\alpha+1-\dfrac{2(3+2\beta+2\alpha\mu+\mu+\Gamma_3)}{(3+2\beta+2\alpha\mu+\mu+\Gamma_3)^2-4\beta^2}-\dfrac{(2\alpha+1)\mu+1+\Gamma_3}{2\mu} \end{cases} \tag{12}$$

where

$$\begin{cases} \Gamma_1 = \sqrt{4\mu^2\alpha^2-8\beta\mu\alpha+4\mu^2\alpha-4\alpha\mu+4\beta^2-4\beta\mu+\mu^2+4\beta+2\mu+1} \\ \Gamma_2 = \sqrt{16\mu^2\alpha^2-16\beta\mu\alpha+8\mu^2\alpha-8\alpha\mu+4\beta^2-4\beta\mu+\mu^2+4\beta+2\mu+1} \\ \Gamma_3 = \sqrt{4\mu^2\alpha^2+4\mu^2\alpha-4\alpha\mu+\mu^2+2\mu+1} \end{cases}$$

The dimensionless eigenvalues for all the bounds presented in Fig. 4 are calculated using Eq. (12). The signs of the eigenvalues are illustrated in Fig. 5, where the upper and lower halves represent positive and negative domains, respectively. The vertical heights of the lines do not represent their magnitudes and have no physical meanings. Different vertical heights are intentionally set to separate the lines. As topological interface states could take place around the transition points, the evolutions of eigenvalues around the transition points are of interest. Around transition point T1 when $\beta < 0$, we have $\lambda_1 > 0$ and $\lambda_3 < 0$ for the intersected bound curves I and III. In contrast, when $\beta > 0$, $\lambda_1 < 0$ and $\lambda_3 > 0$. The eigenvalue evolution trends around transition points T2 and T3 for bound pairs (II, IV) and (V, VI) can be determined from Fig. 5 as well.

Since the signs of the eigenvalues are determined around the transition points, the mode polarization is investigated by examining the eigenvectors. By substituting the eigenvalue Eq. (11) back into Eq. (10), one obtains the eigenvector:

$$\left[\tilde{u}_i \quad \tilde{v}_i \quad \tilde{u}_j \quad \tilde{v}_j\right]^T = \left[\pm e^{I\phi(q)} \quad \left(\pm a e^{I\phi(q)}+b\right) \quad 1 \quad \left(\pm b e^{I\phi(q)}+a\right)\right]^T \tag{13}$$

where

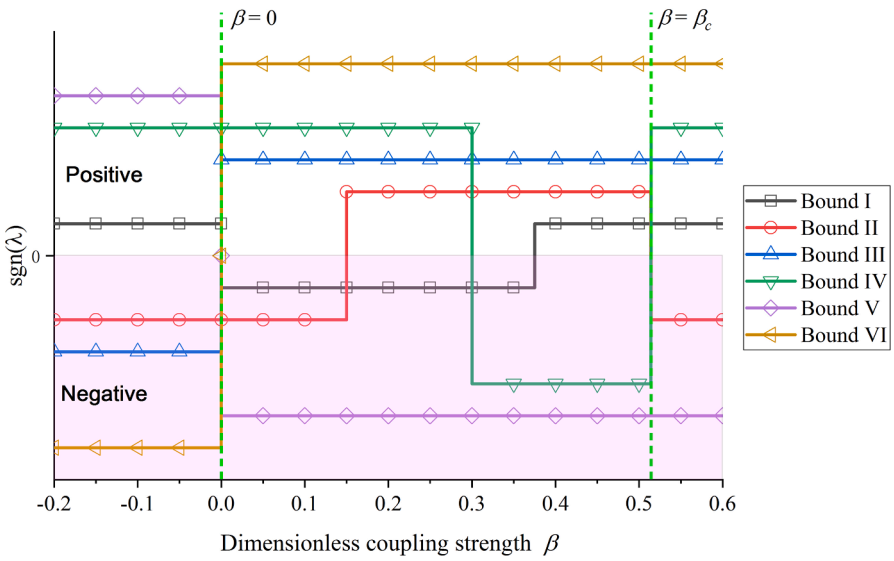

Fig. 5. Dimensionless eigenvalues for all the bands presented in Fig. 4. The upper and lower half graphs represent the positive and negative domains, respectively.

$$\phi(q) = arg\left(\alpha + \alpha e^{-Iq} + \frac{\beta}{\left[\left(\beta + 1 - \Omega_r^2\right)^2 - \beta^2\right]}\right) \tag{14}$$

and arg is the argument operator that takes the phase angle of the complex variable inside. $\phi(q)$ at the Brillouin-zone boundary, i.e., $q = \pi$, becomes

$$\phi(\pi) = arg\left(\frac{\beta}{\left[\left(\beta + 1 - \Omega_r^2\right)^2 - \beta^2\right]}\right) \tag{15}$$

When $\Omega_r < 1$, $\left(\beta + 1 - \Omega_r^2\right)^2 > \beta^2$ implies that the denominator of the complex variable inside the argument operator is always positive. Thus, under the condition of $\Omega_r < 1$, $\phi(\pi)$ equals to 0 or π completely depends on the sign of β. However, when $\Omega_r > 1$, the situation becomes complicated. We temporarily put aside the latter situation and focus on the discussion of the situation when $\Omega_r < 1$ first.

- Transition Point T1

From Fig. 4, it can be noted that around transition point T1, the first band gap always occurs in the low-frequency range that just satisfies the condition $\Omega_r < 1$. Therefore, for the states on bands I and III, we have

$$\begin{cases} \beta > 0 & \rightarrow \quad \phi(\pi)_{\mathrm{I/III}} = 0 \\ \beta < 0 & \rightarrow \quad \phi(\pi)_{\mathrm{I/III}} = \pi \end{cases} \tag{16}$$

On the other hand, from Fig. 5 we have determined the signs of the eigenvalues of the bands I and III around transition point T1. When $\beta > 0$, at state S1 (S1 is the state at the lower bound of the first band gap, as shown in Fig. 3), $\lambda < 0$, we have:

$$\begin{aligned} sgn\left[\widetilde{u}_i \quad \widetilde{v}_i \quad \widetilde{u}_j \quad \widetilde{v}_j\right]^T &= sgn\left[-e^{I\phi(q)} \quad \left(-ae^{I\phi(q)} + b\right) \quad 1 \quad \left(-be^{I\phi(q)} + a\right)\right]^T \\ &= \left[- \quad sgn\left(\Omega_r^2 - 1\right) \quad + \quad sgn\left(1 - \Omega_r^2\right)\right]^T \\ &= [- \quad - \quad + \quad +]^T \end{aligned} \tag{17}$$

When $\beta > 0$, at state S2, $\lambda > 0$, we have:

$$\begin{aligned} sgn\left[\widetilde{u}_i \quad \widetilde{v}_i \quad \widetilde{u}_j \quad \widetilde{v}_j\right]^T &= sgn\left[e^{I\phi(q)} \quad \left(ae^{I\phi(q)} + b\right) \quad 1 \quad \left(be^{I\phi(q)} + a\right)\right]^T \\ &= \left[+ \quad sgn\left(2\beta + 1 - \Omega_r^2\right) \quad + \quad sgn\left(2\beta + 1 - \Omega_r^2\right)\right]^T \\ &= [+ \quad + \quad + \quad +]^T \end{aligned} \tag{18}$$

When $\beta < 0$, at state S1, $\lambda < 0$, we have:

$$\begin{aligned} sgn\left[\widetilde{u}_i \quad \widetilde{v}_i \quad \widetilde{u}_j \quad \widetilde{v}_j\right]^T &= sgn\left[-e^{I\phi(q)} \quad \left(-ae^{I\phi(q)} + b\right) \quad 1 \quad \left(-be^{I\phi(q)} + a\right)\right]^T \\ &= \left[+ \quad sgn\left(2\beta + 1 - \Omega_r^2\right) \quad + \quad sgn\left(2\beta + 1 - \Omega_r^2\right)\right]^T \\ &= [+ \quad + \quad + \quad +]^T \end{aligned} \tag{19}$$

When $\beta < 0$, at state S2, $\lambda > 0$, we have:

$$\begin{aligned} sgn\left[\widetilde{u}_i \quad \widetilde{v}_i \quad \widetilde{u}_j \quad \widetilde{v}_j\right]^T &= sgn\left[e^{I\phi(q)} \quad \left(ae^{I\phi(q)} + b\right) \quad 1 \quad \left(be^{I\phi(q)} + a\right)\right]^T \\ &= \left[- \quad sgn\left(\Omega_r^2 - 1\right) \quad + \quad sgn\left(1 - \Omega_r^2\right)\right]^T \\ &= [- \quad - \quad + \quad +]^T \end{aligned} \tag{20}$$

Table 1 summarizes the signs of the eigenvector elements. Comparing the states at S1/S2 when $\beta > 0$ (Eqs. (17) & (18)) and when $\beta < 0$ (Eqs. (19) & (20)), a mode polarization inversion behaviour is noted. In other words, the two modes related to the states S1 and S2 are exchanged when β changes from negative to positive.

- Transition Point T2

Table 1
Signs of eigenstates at the bounds of the first band gap around transition point T1.

		$\beta > 0$	$\beta < 0$
Transition Point T1 First Band Gap	S1	$[- \quad - \quad + \quad +]^T$	$[+ \quad + \quad + \quad +]^T$
	S2	$[+ \quad + \quad + \quad +]^T$	$[- \quad - \quad + \quad +]^T$

Fig. 4 shows that transition point T2 appears at the place where $\Omega_r \approx 1.265 > 1$ and $\beta_c \approx 0.514 > 0$. Thus, the denominator of Eq. (15) $\left[\left(\beta+1-\Omega_r^2\right)^2-\beta^2\right] < 0$. By following a more meticulous calculation, $\phi(q)$ for Bounds II and IV at the Brillouin-zone boundary, i.e., $q = 0$, is determined

$$\begin{cases} \beta > \beta_c & \rightarrow \quad \phi(0)_{\mathrm{II/IV}} = 0 \\ \beta < \beta_c & \rightarrow \quad \phi(0)_{\mathrm{II/IV}} = \pi \end{cases} \tag{21}$$

As shown in Fig. 5, around transition point T2, when $\beta > \beta_c$, at state S3, $\lambda > 0$, we have:

$$\begin{aligned} sgn\begin{bmatrix} \widetilde{u}_i & \widetilde{v}_i & \widetilde{u}_j & \widetilde{v}_j \end{bmatrix}^T &= sgn\begin{bmatrix} e^{I\phi(q)} & \left(ae^{I\phi(q)}+b\right) & 1 & \left(be^{I\phi(q)}+a\right) \end{bmatrix}^T \\ &= \begin{bmatrix} + & sgn\left(2\beta+1-\Omega_r^2\right) & + & sgn\left(2\beta+1-\Omega_r^2\right) \end{bmatrix}^T \\ &= \begin{bmatrix} + & + & + & + \end{bmatrix}^T \end{aligned} \tag{22}$$

When $\beta > \beta_c$, at state S4, $\lambda < 0$, we have:

$$\begin{aligned} sgn\begin{bmatrix} \widetilde{u}_i & \widetilde{v}_i & \widetilde{u}_j & \widetilde{v}_j \end{bmatrix}^T &= sgn\begin{bmatrix} -e^{I\phi(q)} & \left(-ae^{I\phi(q)}+b\right) & 1 & \left(-be^{I\phi(q)}+a\right) \end{bmatrix}^T \\ &= \begin{bmatrix} - & sgn\left(\Omega_r^2-1\right) & + & sgn\left(1-\Omega_r^2\right) \end{bmatrix}^T \\ &= \begin{bmatrix} - & + & + & - \end{bmatrix}^T \end{aligned} \tag{23}$$

When $\beta < \beta_c$, at state S3, $\lambda > 0$, we have:

$$\begin{aligned} sgn\begin{bmatrix} \widetilde{u}_i & \widetilde{v}_i & \widetilde{u}_j & \widetilde{v}_j \end{bmatrix}^T &= sgn\begin{bmatrix} e^{I\phi(q)} & \left(ae^{I\phi(q)}+b\right) & 1 & \left(be^{I\phi(q)}+a\right) \end{bmatrix}^T \\ &= \begin{bmatrix} - & sgn\left(\Omega_r^2-1\right) & + & sgn\left(1-\Omega_r^2\right) \end{bmatrix}^T \\ &= \begin{bmatrix} - & + & + & - \end{bmatrix}^T \end{aligned} \tag{24}$$

When $\beta < \beta_c$, at state S4, $\lambda < 0$, we have:

$$\begin{aligned} sgn\begin{bmatrix} \widetilde{u}_i & \widetilde{v}_i & \widetilde{u}_j & \widetilde{v}_j \end{bmatrix}^T &= sgn\begin{bmatrix} -e^{I\phi(q)} & \left(-ae^{I\phi(q)}+b\right) & 1 & \left(-be^{I\phi(q)}+a\right) \end{bmatrix}^T \\ &= \begin{bmatrix} + & sgn\left(2\beta+1-\Omega_r^2\right) & + & sgn\left(2\beta+1-\Omega_r^2\right) \end{bmatrix}^T \\ &= \begin{bmatrix} + & + & + & + \end{bmatrix}^T \end{aligned} \tag{25}$$

Table 2 summarizes the signs of the eigenvector elements of the two states around transition point T2. Similar to the situation around transition point T1, the mode polarization directions are inversed after crossing transition point T2. Therefore, it can be deduced that transition point T2 should also support the generation of a topological interface state in the second band gap.

- Transition Point T3

Regarding transition point T3 shown in Fig. 4, it appears at the place where $\Omega_r \approx 1.507 > 1$ and $\beta = 0$. Thus, the denominator of Eq. (15) $\left[\left(\beta+1-\Omega_r^2\right)^2-\beta^2\right] > 0$. $\phi(q)$ for Bounds V and VI at the Brillouin-zone boundary, i.e., $q = \pi$, becomes

$$\begin{cases} \beta > 0 & \rightarrow \quad \phi(\pi)_{\mathrm{V/VI}} = 0 \\ \beta < 0 & \rightarrow \quad \phi(\pi)_{\mathrm{V/VI}} = \pi \end{cases} \tag{26}$$

Eq. (26) becomes the same as Eq. (16). From Fig. 5, it can be noted that the eigenvalue sign variation around transition point T3 is also the same as that around transition point T1. Therefore, the situation around transition point T3 is exactly like that around transition point T1. This can be further confirmed by inspecting the signs of the eigenvector elements summarized in Table 3. In other words, transition point T3 also opens an opportunity for producing a topological interface state in the third band gap.

4.3. Zak phase calculation

In this subsection, the topological characteristics of the bands are identified by calculating the topological invariant, i.e., the Zak phase, which is defined as:

Table 2
Signs of eigenstates at the bounds of the second band gap around transition point T2.

		$\beta > \beta_c$	$\beta < \beta_c$
Transition Point T2 Second Band Gap	S3	$[+ \ + \ + \ +]^T$	$[- \ + \ + \ -]^T$
	S4	$[- \ + \ + \ -]^T$	$[+ \ + \ + \ +]^T$

Table 3
Signs of eigenstates at the bounds of the third band gap around transition point T3.

		$\beta > 0$	$\beta < 0$
Transition Point T3 Third Band Gap	S5	$[-\ -\ +\ +]^T$	$[+\ +\ +\ +]^T$
	S6	$[+\ +\ +\ +]^T$	$[-\ -\ +\ +]^T$

$$\theta = I\int_{-\pi}^{\pi} dq\langle\Psi|\partial_q|\Psi\rangle \tag{27}$$

Differentiating the displacement eigenvector by the time gives the velocity eigenvector:

$$\frac{d}{dt}\left[\widetilde{u}_i \quad \widetilde{v}_i \quad \widetilde{u}_j \quad \widetilde{v}_j\right]^T = \left[\pm I\Omega_r e^{I\phi(q)} \quad I\Omega_r\left(\pm ae^{I\phi(q)} + b\right) \quad I\Omega_r \quad I\Omega_r\left(\pm be^{I\phi(q)} + a\right)\right]^T \tag{28}$$

We normalize the eigenvector by the energy to convert it into the Hamiltonian form:

$$\begin{aligned}|\Psi\rangle &= \frac{\left[\pm\mu e^{I\phi(q)} \quad \left(\pm ae^{I\phi(q)} + b\right) \quad \mu \quad \left(\pm be^{I\phi(q)} + a\right)\right]^T}{\sqrt{2a^2\mu^2 + 2b^2\mu^2 + 2 \pm 4ab\mu^2 cos\phi(q)}} \\ &= \left[\pm C(q)e^{i\phi(q)} \quad \left(\pm A(q)e^{i\phi(q)} + B(q)\right) \quad C(q) \quad \left(\pm B(q)e^{i\phi(q)} + A(q)\right)\right]^T\end{aligned} \tag{29}$$

where $2A^2(q) + 2B^2(q) + 2C^2(q) \pm 4ABcos\phi(q) = 1$. Substituting Eq. (29) into Eq. (27) yields:

$$\begin{aligned}\theta &= I\int_{-\pi}^{\pi}\left\{\begin{array}{c}\left[\pm C(q)e^{I\phi(q)}\right]^*\dfrac{\partial\left[\pm C(q)e^{I\phi(q)}\right]}{\partial q} \\ +\left[\pm A(q)e^{I\phi(q)} + B(q)\right]^*\dfrac{\partial\left[\pm A(q)e^{I\phi(q)} + B(q)\right]}{\partial q} \\ +C(q)\dfrac{\partial C(q)}{\partial q} + \left[\pm B(q)e^{I\phi(q)} + A(q)\right]^*\dfrac{\partial\left[\pm B(q)e^{I\phi(q)} + A(q)\right]}{\partial q}\end{array}\right\}dq \\ &= I\int_{-\pi}^{\pi}\left\{\begin{array}{c}\left[C(q)e^{I\phi(q)}\right]^*\left[\dfrac{\partial C(q)}{\partial q}e^{I\phi(q)} + C(q)I\dfrac{\partial\phi(q)}{\partial q}e^{I\phi(q)}\right] \\ +\left[\pm A(q)e^{I\phi(q)} + B(q)\right]^*\left[\dfrac{\partial(\pm A(q))}{\partial q}e^{I\phi(q)} \pm A(q)I\dfrac{\partial\phi(q)}{\partial q}e^{I\phi(q)} + \dfrac{\partial B(q)}{\partial q}\right] \\ +C(q)\dfrac{\partial C(q)}{\partial q} + \left[\pm B(q)e^{I\phi(q)} + A(q)\right]^*\left[\dfrac{\partial(\pm B(q))}{\partial q}e^{I\phi(q)} \pm B(q)I\dfrac{\partial\phi(q)}{\partial q}e^{I\phi(q)} + \dfrac{\partial A(q)}{\partial q}\right]\end{array}\right\}dq \\ &= \frac{I}{2}\int_{-\pi}^{\pi}\left\{\begin{array}{c}\dfrac{\partial\left[2A^2(q) + 2B^2(q) + 2C^2(q) \pm 4ABcos\phi(q)\right]}{\partial q} \\ +\left[2A^2(q) + 2B^2(q) + 2C^2(q) \pm 4A(q)B(q)cos\phi(q)\right]I\dfrac{\partial\phi(q)}{\partial q}\end{array}\right\}dq \\ &= -\frac{1}{2}\int_{-\pi}^{\pi}\left\{\frac{\partial\phi(q)}{\partial q}\right\}dq \\ &= -\frac{1}{2}[\phi(\pi) - \phi(-\pi)]\end{aligned} \tag{30}$$

Note that $\phi(q) = arg\left(\alpha + \alpha e^{-Iq} + \beta/\left[\left(\beta + 1 - \Omega_r^2\right)^2 - \beta^2\right]\right)$ is an Ω_r-dependent function. The Zak phases for different bands need to be computed separately. For the cases shown in Fig. 3.(a) and (c), the Zak phases of the four bands are all equal to π when $\beta < 0$, and equal to 0 when $\beta > 0$.

To know whether topological interface states can appear in a specific band gap, the below figure of merit could be utilized to make a judgment.

$$sgn\left[\zeta^{(n)}\right] = (-1)^n exp\left(I\sum_{m=0}^{n-1}\theta^{(m)}\right) \tag{31}$$

For the n^{th} band gap, if the LHS and RHS *meta*-chains of the topological metamaterial have different computed signs, i.e., $sgn\left[\zeta^{(n)}\right]$ is

different for LHS and RHS, topological interface states will definitely appear [16]. Otherwise, topological interface states will not appear.

Table 4 lists the determined signs of $\zeta^{(n)}$ for the band gaps shown in Fig. 3.(a) and (c). It is worth noting that the two metamaterials corresponding to Fig. 3.(a) and (c) are, respectively, on the two sides of transition points T1 & T3. According to the aforementioned criterion, the topological interface states should appear in the first and the third band gaps but not in the second band gap. It is confirmed that the result of Zak phase calculation agrees with the polarization transition analysis.

Subsequently, the Zak phase analysis is performed for two selected metamaterials on the two sides of transition point T2. The determined signs of $\zeta^{(n)}$ for the band gaps of the two metamaterials are listed in Table 5. Unlike the situation around transition points T1 & T3, It can be found that $sgn\left[\zeta^{(n)}\right]$ only differs in the second band gap, which indicates that the topological interface can only exist in the second band gap. The previous polarization transition analysis around transition point T2 agrees with this prediction and unveils the underlying mechanism from the modal perspective.

5. Interface states formation

The analyses in the previous section predict the existence of topological interface states in the internally coupled metamaterial. In this section, topological metamaterials that satisfy previously derived conditions are constructed to directly demonstrate the topological interface states through the supercell analysis.

5.1. Band gap matching condition

In the previous sections, all the system parameters are non-dimensionlized with reference to the local resonator. However, the purpose of this work is to propose a locally resonant topological metamaterial with a uniform host structure, as shown in Fig. 6. Hence, to keep the analysis still in the dimensionless form but with reference to the outer mass-spring chain, i.e., to assume a fixed and uniform host structure, a new set of dimensionless parameters are introduced as follows.

$$\begin{cases} \mu = \dfrac{m}{M} & \alpha_0 = \dfrac{K_2}{K_1} \quad \beta_0 = \dfrac{K}{K_1} \quad \gamma = \dfrac{k}{K_1} \\ \Omega = \dfrac{\omega}{\sqrt{K_1/M}} & \widetilde{U} = \dfrac{U}{L} \quad \widetilde{F} = \dfrac{F}{K_1 L} \end{cases} \tag{32}$$

The relationships between this set of dimensionless parameters and the previous set (i.e., Eq. (2)) are:

$$\alpha_1 = \frac{1}{\gamma}; \quad \alpha_2 = \frac{\alpha_0}{\gamma}; \quad \beta = \frac{\beta_0}{\gamma} \tag{33}$$

Using the above relationships, i.e., Eq. (33), the formulas derived in the previous sections can be transformed into the forms that abide by the new dimensionless framework. To activate an interface state in the first band gap of the topological metamaterial (Fig. 6), the first band gaps of the left-hand side (LHS) and the right-hand side (RHS) metamaterial chains (*meta*-chains) need to have an interaction. Unlike an ordinary diatomic metamaterial presented in [16], simply changing the sign of the coupling strength β will lead to two completely misaligned band gaps with no interaction. Therefore, band gap matching conditions are sought to overlap the band gaps in the LHS and RHS *meta*-chains first. Hereinafter, the subscripts LHS and RHS are introduced to indicate the parameters related to the LHS and RHS *meta*-chains, respectively. For example, k_{LHS} and k_{RHS} denote the stiffness constants of the local resonators attached to the LHS and RHS *meta*-chains, respectively. β_{LHS} and β_{RHS} represent the dimensionless coupling strength (β) implemented in the LHS and RHS *meta*-chains, respectively.

We assume that the outer mass-spring chain is uniform, having the same mass and spring constant, i.e., $\alpha_0 = 1$. The values of β for the LHS and RHS *meta*-chains should be determined according to Fig. 4: β_{LHS} and β_{RHS} should be selected, respectively, from the left and right sides of a transition point. The local resonators on the LHS and RHS could be adapted to meet the band gap matching condition. Once the parameters of the LHS *meta*-chain, i.e., μ_{LHS} and γ_{LHS}, are given, matching the first band gap becomes seeking for real solutions of μ_{RHS} and γ_{RHS} to satisfy the following equation set:

Table 4
Signs of $\zeta^{(n)}$ for the band gaps shown in Fig. 3(a) and (c).

	$\beta < 0$ Fig. 3(a)	$\beta > 0$ Fig. 3(c)
$sgn\left[\zeta^{(\mathrm{I})}\right]$	+	−
$sgn\left[\zeta^{(\mathrm{II})}\right]$	+	+
$sgn\left[\zeta^{(\mathrm{III})}\right]$	+	−

Table 5
Signs of $\varsigma^{(n)}$ for the band gaps of two selected metamaterials on the two sides of transition point T2.

	$\beta < \beta_c$	$\beta > \beta_c$
$sgn[\zeta^{(\mathrm{I})}]$	−	−
$sgn[\zeta^{(\mathrm{II})}]$	+	−
$sgn[\zeta^{(\mathrm{III})}]$	+	+

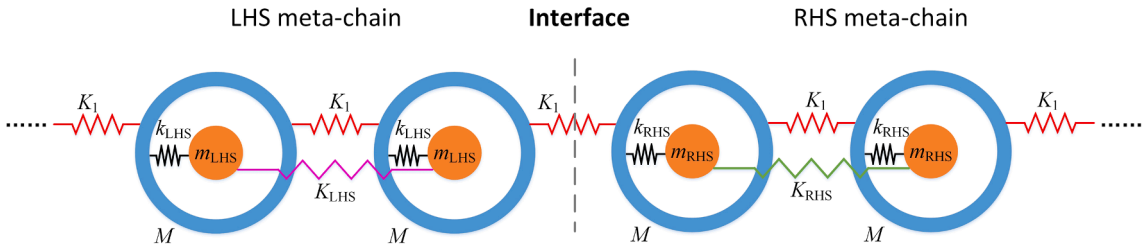

Fig. 6. A locally resonant topological metamaterial that is assembled by two types of metamaterial chains on the left and right hand sides, respectively. The host structure, i.e., the outer mass-spring chain is kept uniform.

$$\begin{cases} \sqrt{\dfrac{\gamma_{\mathrm{LHS}}}{\mu_{\mathrm{LHS}}}} \times f_{\mathrm{I}}^{\mathrm{LHS}}\left(\mu=\mu_{\mathrm{LHS}},\ \alpha=\dfrac{1}{\gamma_{\mathrm{LHS}}},\ \beta=\beta_{\mathrm{LHS}}\right) = \sqrt{\dfrac{\gamma_{\mathrm{RHS}}}{\mu_{\mathrm{RHS}}}} \times \mathrm{f}_{\mathrm{III}}^{\mathrm{RHS}}\left(\mu=\mu_{\mathrm{RHS}},\ \alpha=\dfrac{1}{\gamma_{\mathrm{RHS}}},\ \beta=\beta_{\mathrm{RHS}}\right) \\ \sqrt{\dfrac{\gamma_{\mathrm{LHS}}}{\mu_{\mathrm{LHS}}}} \times f_{\mathrm{III}}^{\mathrm{LHS}}\left(\mu=\mu_{\mathrm{LHS}},\ \alpha=\dfrac{1}{\gamma_{\mathrm{LHS}}},\ \beta=\beta_{\mathrm{LHS}}\right) = \sqrt{\dfrac{\gamma_{\mathrm{RHS}}}{\mu}} \times f_{\mathrm{I}}^{\mathrm{RHS}}\left(\mu=\mu_{\mathrm{RHS}},\ \alpha=\dfrac{1}{\gamma_{\mathrm{RHS}}},\ \beta=\beta_{\mathrm{RHS}}\right) \end{cases} \tag{34}$$

In the above equations, $\beta=\beta_{\mathrm{LHS}}$ in the bracket means a substitution operator, i.e., replacing β by β_{LHS} in the expression of $f_{\mathrm{I}}^{\mathrm{LHS}}$. It is worth noting that a perfect match between the two band gaps is a sufficient but unnecessary condition. Similarly, the matching conditions for the second and third band gaps in the LHS and RHS *meta*-chains are given in Eq. (35) and (36), respectively.

$$\begin{cases} \sqrt{\dfrac{\gamma_{\mathrm{LHS}}}{\mu_{\mathrm{LHS}}}} \times f_{\mathrm{II}}^{\mathrm{LHS}}\left(\mu=\mu_{\mathrm{LHS}},\ \alpha=\dfrac{1}{\gamma_{\mathrm{LHS}}},\ \beta=\beta_{\mathrm{LHS}}\right) = \sqrt{\dfrac{\gamma_{\mathrm{RHS}}}{\mu_{\mathrm{RHS}}}} \times f_{\mathrm{IV}}^{\mathrm{RHS}}\left(\mu=\mu_{\mathrm{RHS}},\ \alpha=\dfrac{1}{\gamma_{\mathrm{RHS}}},\ \beta=\beta_{\mathrm{RHS}}\right) \\ \sqrt{\dfrac{\gamma_{\mathrm{LHS}}}{\mu_{\mathrm{LHS}}}} \times f_{\mathrm{IV}}^{\mathrm{LHS}}\left(\mu=\mu_{\mathrm{LHS}},\ \alpha=\dfrac{1}{\gamma_{\mathrm{LHS}}},\ \beta=\beta_{\mathrm{LHS}}\right) = \sqrt{\dfrac{\gamma_{\mathrm{RHS}}}{\mu}} \times f_{\mathrm{II}}^{\mathrm{RHS}}\left(\mu=\mu_{\mathrm{RHS}},\ \alpha=\dfrac{1}{\gamma_{\mathrm{RHS}}},\ \beta=\beta_{\mathrm{RHS}}\right) \end{cases} \tag{35}$$

$$\begin{cases} \sqrt{\dfrac{\gamma_{\mathrm{LHS}}}{\mu_{\mathrm{LHS}}}} \times f_{\mathrm{V}}^{\mathrm{LHS}}\left(\mu=\mu_{\mathrm{LHS}},\ \alpha=\dfrac{1}{\gamma_{\mathrm{LHS}}},\ \beta=\beta_{\mathrm{LHS}}\right) = \sqrt{\dfrac{\gamma_{\mathrm{RHS}}}{\mu_{\mathrm{RHS}}}} \times \mathrm{f}_{\mathrm{VI}}^{\mathrm{RHS}}\left(\mu=\mu_{\mathrm{RHS}},\ \alpha=\dfrac{1}{\gamma_{\mathrm{RHS}}},\ \beta=\beta_{\mathrm{RHS}}\right) \\ \sqrt{\dfrac{\gamma_{\mathrm{LHS}}}{\mu_{\mathrm{LHS}}}} \times f_{\mathrm{VI}}^{\mathrm{LHS}}\left(\mu=\mu_{\mathrm{LHS}},\ \alpha=\dfrac{1}{\gamma_{\mathrm{LHS}}},\ \beta=\beta_{\mathrm{LHS}}\right) = \sqrt{\dfrac{\gamma_{\mathrm{RHS}}}{\mu}} \times f_{\mathrm{V}}^{\mathrm{RHS}}\left(\mu=\mu_{\mathrm{RHS}},\ \alpha=\dfrac{1}{\gamma_{\mathrm{RHS}}},\ \beta=\beta_{\mathrm{RHS}}\right) \end{cases} \tag{36}$$

5.2. *Transfer matrix method for supercell analysis*

To construct a supercell for verifying the previous predictions, the transfer matrix (TM) method is employed [31]. Fig. 7 shows the schematic of a unit cell with sketches for illustrating the force/displacement transfer from the left to the right ends. The right end

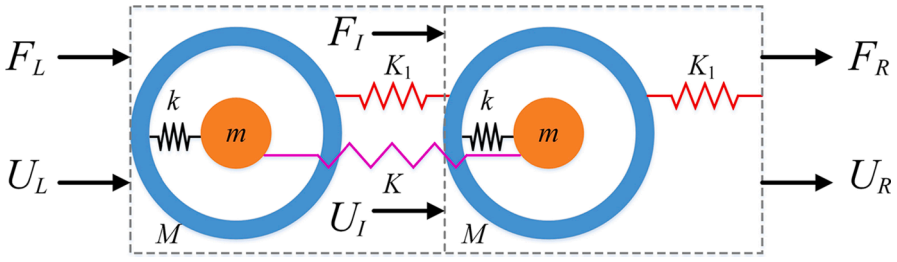

Fig. 7. Schematic of the internally metamaterial with sketches for illustrating the force/displacement transfer from the left to the right ends of the unit cell.

variables can be expressed using the left end variables:

$$\begin{bmatrix} F_R \\ U_R \end{bmatrix} = \underbrace{\left\{ \begin{bmatrix} C_{11} & C_{12} \\ C_{21} & C_{22} \end{bmatrix} \begin{bmatrix} B_{11} & B_{12} \\ B_{21} & B_{22} \end{bmatrix} + \begin{bmatrix} D_{11} & D_{12} \\ D_{21} & D_{22} \end{bmatrix} \right\}}_{\mathbf{T}} \begin{bmatrix} F_L \\ U_L \end{bmatrix} \tag{37}$$

The explicit expressions of the elements in the coefficient matrices can be found in the Appendix. For a topological metamaterial that contains multiple cells, the global transfer matrix that relates the variables on the LHS and RHS ends can be constructed as:

$$\begin{bmatrix} F_{\mathrm{LHS}} \\ U_{\mathrm{LHS}} \end{bmatrix} = \mathbf{T}_{\mathrm{g}} \begin{bmatrix} \mathrm{F_{RHS}} \\ \mathrm{U_{RHS}} \end{bmatrix} = \mathbf{T}_{\mathrm{LHS}}^{\mathrm{n}} \mathbf{T}_{\mathrm{RHS}}^{\mathrm{n}} \begin{bmatrix} \mathrm{F_{RHS}} \\ \mathrm{U_{RHS}} \end{bmatrix} \tag{38}$$

where the subscript g denotes the global transfer matrix. The subscripts LHS and RHS denote the unit cells in the LHS and RHS *meta*-chains, respectively. The LHS and RHS *meta*-chains are assumed to have the same number of unit cells – n. Because of the periodicity, the LHS and RHS variables are governed by the following periodic condition according to the Bloch's theorem:

$$\begin{bmatrix} F_{\mathrm{LHS}} \\ U_{\mathrm{LHS}} \end{bmatrix} = \begin{bmatrix} e^{Iq} & 0 \\ 0 & e^{Iq} \end{bmatrix} \begin{bmatrix} F_{\mathrm{RHS}} \\ U_{\mathrm{RHS}} \end{bmatrix} \tag{39}$$

Substituting Eq. (38) into Eq. (39) yields an eigenvalue problem:

$$\left| \mathbf{T}_{\mathrm{g}} - e^{Iq} \mathbf{I} \right| = 0 \tag{40}$$

Solving Eq. (40) gives the dispersion relation of the supercell.

On the other hand, by applying appropriate boundary conditions, the transmittance spectrum of a single supercell could be calculated. For example, let the excitation be input from the left end in the form of a unit displacement, and the right end is let free.

$$\begin{cases} U_{\mathrm{LHS}} = 1 \\ F_{\mathrm{RHS}} = 0 \end{cases} \tag{41}$$

Substituting Eq. (41) into Eq. (38), two linear equations of two unknown variables, i.e., U_{RHS} and F_{LHS}, are obtained. Solving the equation set, the transmittance could then be computed according to the following definition:

$$\tau = 20 log_{10} \left(\frac{|U_{\mathrm{RHS}}|}{|U_{\mathrm{LHS}}|} \right) \tag{42}$$

where τ is in the unit of dB.

- Topological interface state in the first band gap

To demonstrate the interface states formation in the first band gap of the topological metamaterial, we fix the parameters of the LHS *meta*-chain as: $\mu_{\mathrm{LHS}} = 0.6$, $\alpha_0 = 1$, $\gamma_{\mathrm{LHS}} = 1$, and $\beta_{\mathrm{LHS}} = 0.1$. Using the band gap matching condition, i.e., Eq. (34) , the parameters of the RHS *meta*-chain are determined to be: $\mu_{\mathrm{RHS}} = 0.482$, $\alpha_0 = 1$, $\gamma_{\mathrm{RHS}} = 1.372$, and $\beta_{\mathrm{RHS}} = -0.07$. It is worth mentioning that as the non-dimensionlization is performed by taking reference to the host structure, it implies that the host structure parameters are remained unchanged and uniform. The local resonator configurations of the LHS and RHS *meta*-chains are engineered to realize the band gap

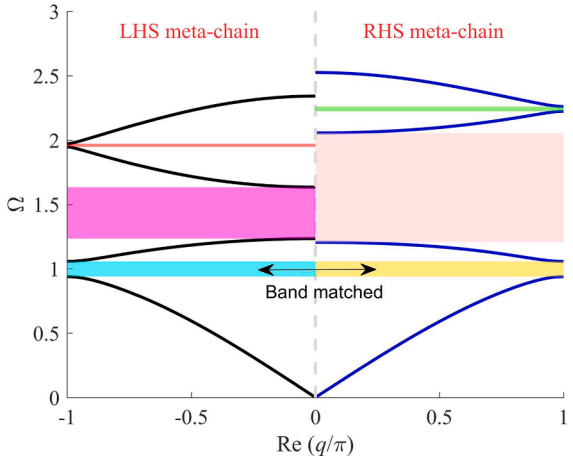

Fig. 8. Comparison of the band structures of the LHS *meta*-chain and the RHS *meta*-chain. The colour shaded areas denote the band gaps. The LHS *meta*-chain is tuned with the parameters of $\mu_{\mathrm{LHS}} = 0.6$, $\alpha_0 = 1$, $\gamma_{\mathrm{LHS}} = 1$, and $\beta_{\mathrm{LHS}} = 0.1$. The RHS *meta*-chain is tuned with the parameters of $\mu_{\mathrm{LHS}} = 0.482$, $\alpha_0 = 1$, $\gamma_{\mathrm{LHS}} = 1.372$, and $\beta_{\mathrm{LHS}} = -0.07$.

matching condition. Fig. 8 compares the band structures of the two *meta*-chains. As expected, their first band gaps tightly overlap with each other.

Fig. 9(a) shows the band structure of the topological metamaterial that is constructed by assembling the two types of metamaterial chains. Each metamaterial chain contains 10 unit cells. In the first band gap, there appears a flat band (i.e., the red line) that corresponds to the topological interface state. The transmittance spectrum of the topological metamaterial is plotted in Fig. 9.(b). The black solid and blue dashed lines represent the results when the excitations are applied from the left and right ends, respectively. It can be noted that a sharp transmittance peak appears in the first attenuation region that corresponds to the first band gap. Regardless of the excitation direction, the transmittance peak always occurs at the same frequency that is identical to the interface state frequency marked in Fig. 9.(a).

The displacement distribution along the entire topological metamaterial chain is presented in Fig. 10 to demonstrate what exactly happens at the interface state. The *y*-axis represents the normalized displacement with reference to the maximum one of all the outer masses. It can be seen that regardless of the excitation direction, the 21-th outer mass undergoes an oscillation with the maximum amplitude, indicating the energy localization at the interface.

- Topological interface state in the second band gap

To meet the requirements for the occurrence of the interface state in the second band gap, the parameters of the LHS *meta*-chain are tuned to $\mu_{\mathrm{LHS}} = 0.6$, $\alpha_0 = 1$, $\gamma_{\mathrm{LHS}} = 1$, and $\beta_{\mathrm{LHS}} = 0.7$. The parameters of the RHS *meta*-chain are tuned to $\mu_{\mathrm{RHS}} = 0.567$, $\alpha_0 = 1$, $\gamma_{\mathrm{RHS}} = 1.128$, and $\beta_{\mathrm{RHS}} = 0.4$ to overlap its second band with that of the LHS *meta*-chain. Fig. 11 compares the band structures of the two *meta*-chains. It is noted that their second band gaps overlap with each other tightly. Their first/third band gaps also intersect, but not seamlessly.

A supercell lattice of the topological metamaterial is constructed by connecting the LHS and RHS *meta*-chains. The periods of both the LHS and RHS *meta*-chains are the same of 10 unit cells. Fig. 12 shows the band structure and the transmittance spectrum of the constructed topological metamaterial. As shown in Fig. 12.(a), a flat red band appears in the second band gap, indicating the emergence of the interface state. At the corresponding frequency, a sharp peak is observed in the transmittance spectrum presented in Fig. 12.(b). Regardless of the excitation direction, the sharp peak remains at the same frequency. Besides, one may notice that though the first and third band gaps are also intersected, no interface states are produced in either band gap. The small peaks in the first and the third band gaps are not formed by interfaces states. For the small peaks near the band gap bounds, they are formed due to the band gap mismatch. The vibration attenuation capability of the mismatched band gap portion is not sufficiently strong. As the transmittance spectrum is calculated for a single supercell, there form a collection of small peaks in the mismatched band gap range. Two other peaks adhering to the transmittance curve obtained under the excitation from right end are formed due to the boundary condition. That is why when the excitation direction is changed from the left end, the two peaks in the band gaps disappear. In summary, the above result agrees with the previous prediction based on the Zak phase calculation results (Table 5).

The displacement distributions of the outer masses along the topological metamaterial are plotted in Fig. 13. Compared to that presented in Fig. 10, it is found that the energy localization effects of both interface states are almost the same: the vibration amplitude at the interface reaches the maximum. The displacement distribution profile is different and the energy localization effect is not as

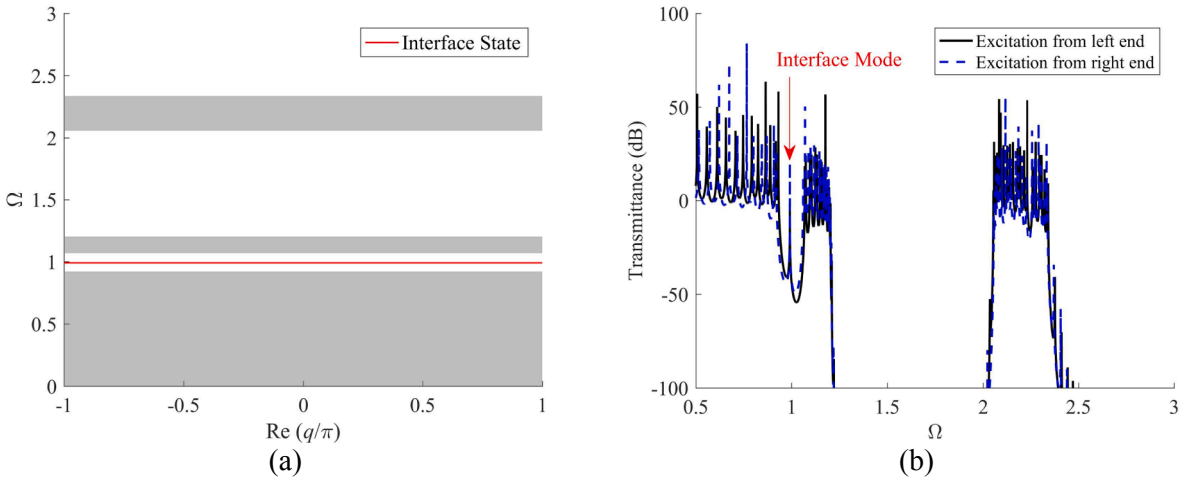

Fig. 9. (a) Band structure of the topological metamaterial, i.e., a supercell system that is constructed by assembling two types of metamaterial chains. Each metamaterial chain contains 10 unit cells. The red line indicates the appearance of the topological interface state in the band gap. (b) The transmittance spectrum of the corresponding topological metamaterial with a single supercell. The black solid line and the blue dashed line represent the results when the excitations are applied from the left and the right ends, respectively. The LHS *meta*-chain is tuned with the parameters of $\mu_{\mathrm{LHS}} = 0.6$, $\alpha_0 = 1$, $\gamma_{\mathrm{LHS}} = 1$, and $\beta_{\mathrm{LHS}} = 0.1$. The RHS *meta*-chain is tuned with the parameters of $\mu_{\mathrm{LHS}} = 0.482$, $\alpha_0 = 1$, $\gamma_{\mathrm{LHS}} = 1.372$, and $\beta_{\mathrm{LHS}} = -0.07$.

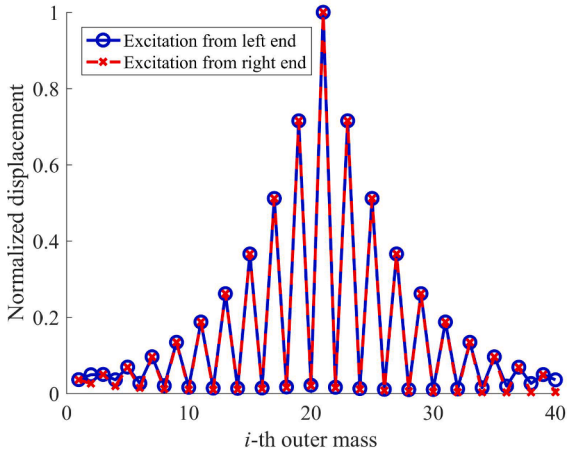

Fig. 10. Displacement distribution along the entire topological metamaterial chain. The *x*-axis denotes the number of the outer mass. The *y*-axis is the normalized displacement. The LHS *meta*-chain is tuned with the parameters of $\mu_{\mathrm{LHS}} = 0.6$, $\alpha_0 = 1$, $\gamma_{\mathrm{LHS}} = 1$, and $\beta_{\mathrm{LHS}} = 0.1$. The RHS *meta*-chain is tuned with the parameters of $\mu_{\mathrm{LHS}} = 0.482$, $\alpha_0 = 1$, $\gamma_{\mathrm{LHS}} = 1.372$, and $\beta_{\mathrm{LHS}} = -0.07$.

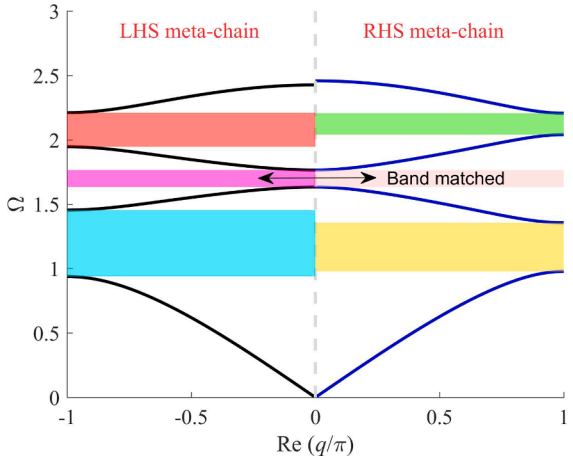

Fig. 11. Comparison of the band structures of the LHS *meta*-chain and the RHS *meta*-chain. The colour shaded areas denote the band gaps. The LHS *meta*-chain is tuned with the parameters of $\mu_{\mathrm{LHS}} = 0.6$, $\alpha_0 = 1$, $\gamma_{\mathrm{LHS}} = 1$, and $\beta_{\mathrm{LHS}} = 0.7$. The RHS *meta*-chain is tuned with the parameters of $\mu_{\mathrm{RHS}} = 0.567$, $\alpha_0 = 1$, $\gamma_{\mathrm{RHS}} = 1.128$, and $\beta_{\mathrm{RHS}} = 0.4$.

obvious as that presented in Fig. 10, since the vibration attenuation capability of the second band gap is much higher than that of the first band gap of the topological metamaterial that corresponds to the result in Fig. 9. The transmittance level in the second band gap shown in Fig. 12.(b) is about −100 dB and the transmittance level in the first band gap shown in Fig. 9.(b) is only about −50 dB. Therefore, the energy can be transmitted to the interface is much less for the case presented in Fig. 13. The reason why the displacement distributions are different when the excitation direction is changed can be found by investigating the vibration capabilities of the LHS and RHS *meta*-chains. The LHS *meta*-chain has a better vibration attenuation capability, thus when the excitation is fed from the left end, it is more difficult for the wave energy to reach the interface. Putting aside these issues, the energy localization effect shown in Fig. 13 can be regarded as the symptom of the interface state formation. It is worth noting that though the energy localization phenomena shown in Fig. 9 and Fig. 12 are similar, the mode polarization behaviours corresponding to the two interface states are actually different. It indicates that provided the polarization transition successfully takes place, a localization effect would appear in the topological metamaterial, leading to the occurrence of the interface state. This formation mechanism guarantees the robustness of the topological interface state.

- Topological interface state in the third band gap

We now proceed to the validation of the topological interface state in the third band gap. The parameters of the LHS *meta*-chain are still kept as: $\mu_{\mathrm{LHS}} = 0.6$, $\alpha_0 = 1$, $\gamma_{\mathrm{LHS}} = 1$. The dimensionless coupling strength is tuned to $\beta_{\mathrm{LHS}} = 0.3$ to produce a third band gap with a considerable width. Based on band gap matching condition, i.e., Eq. (36), the parameters of the RHS *meta*-chain are determined to be:

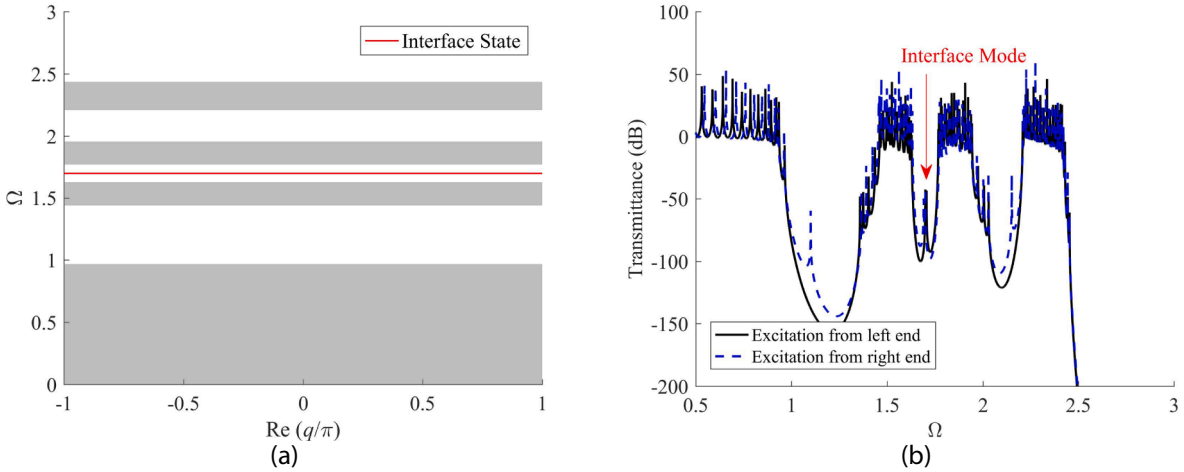

Fig. 12. (a) Band structure of the topological metamaterial, i.e., a supercell system that is constructed by assembling two types of metamaterial chains. Each metamaterial chain contains 10 unit cells. The red line indicates the appearance of the topological interface state in the band gap. (b) The transmittance spectrum of the corresponding topological metamaterial with a single supercell. The black solid line and the blue dashed line represent the results when the excitations are applied from the left and the right ends, respectively. The LHS *meta*-chain is tuned with the parameters of $\mu_{\mathrm{LHS}} = 0.6$, $\alpha_0 = 1$, $\gamma_{\mathrm{LHS}} = 1$, and $\beta_{\mathrm{LHS}} = 0.7$. The RHS *meta*-chain is tuned with the parameters of $\mu_{\mathrm{RHS}} = 0.567$, $\alpha_0 = 1$, $\gamma_{\mathrm{RHS}} = 1.128$, and $\beta_{\mathrm{RHS}} = 0.4$.

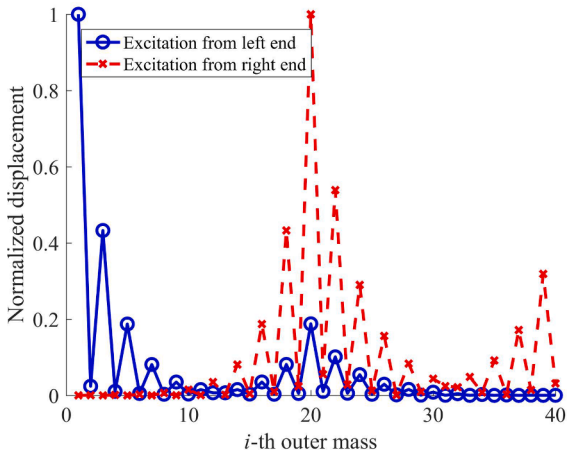

Fig. 13. Displacement distribution along the entire topological metamaterial chain. The *x*-axis denotes the number of the outer mass. The *y*-axis is the normalized displacement. The LHS *meta*-chain is tuned with the parameters of $\mu_{\mathrm{LHS}} = 0.6$, $\alpha_0 = 1$, $\gamma_{\mathrm{LHS}} = 1$, and $\beta_{\mathrm{LHS}} = 0.7$. The RHS *meta*-chain is tuned with the parameters of $\mu_{\mathrm{RHS}} = 0.567$, $\alpha_0 = 1$, $\gamma_{\mathrm{RHS}} = 1.128$, and $\beta_{\mathrm{RHS}} = 0.4$.

$\mu_{\mathrm{RHS}} = 0.486$, $\alpha_0 = 1$, $\gamma_{\mathrm{RHS}} = 1.035$, and $\beta_{\mathrm{RHS}} = -0.3$. Fig. 14 compares the band gaps of the LHS and RHS *meta*-chains using the designed parameters. It is noted that the third band gaps of both metamaterial chains become tightly overlapped.

The band structure and the transmittance spectrum of the supercell lattice of the topological metamaterial constructed using the new LHS and RHS *meta*-chains are examined in Fig. 15.(a) and (b). The flat band (i.e., red line) that exists in the third band gap of the topological metamaterial indicates the appearance of the topological interface state. Moreover, at the same frequency in the transmittance spectrum, a sharp peak that corresponds to the interface state is observed inside an attenuation region induced by the third band gap. No matter whether the excitation is applied from the left or the right end, the sharp peak always exists at the same frequency. On the other hand, one may notice a bundle of small peaks in the second band gap. Their formation can be explained by the band gap mismatch. The mismatched band gap range (as marked in Fig. 14) has a relatively weaker vibration attenuation capability. As the transmittance spectrum comes from a single supercell, the mismatch band gap range cannot perfectly prevent the formation of those small peaks.

The displacement distribution of the topological metamaterial at the interface state in the third band gap is plotted in Fig. 16 to demonstrate the energy localization effect. Similar to the interface states in the first and second band gaps (Fig. 10 and Fig. 13), the macroscopic phenomenon of the energy localization effect brought by the interface state in the third band gap is the same as expected.

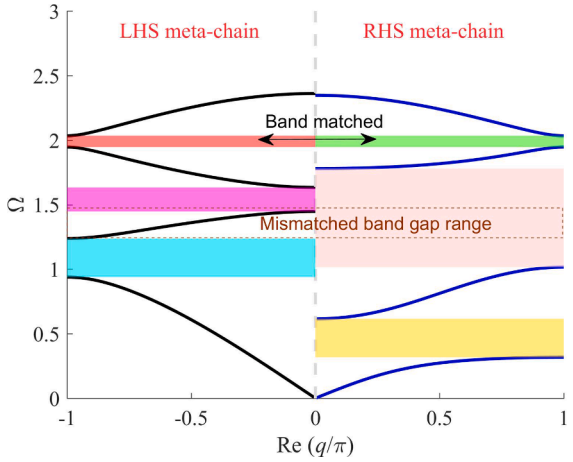

Fig. 14. Comparison of the band structures of the LHS *meta*-chain and the RHS *meta*-chain. The colour shaded areas denote the band gaps. The LHS metamaterial chain is tuned with the parameters of $\mu_{\mathrm{LHS}} = 0.6$, $\alpha_0 = 1$, $\gamma_{\mathrm{LHS}} = 1$, and $\beta_{\mathrm{LHS}} = 0.3$. The RHS *meta*-chain is tuned with the parameters of $\mu_{\mathrm{LHS}} = 0.486$, $\alpha_0 = 1$, $\gamma_{\mathrm{LHS}} = 1.035$, and $\beta_{\mathrm{LHS}} = -0.3$.

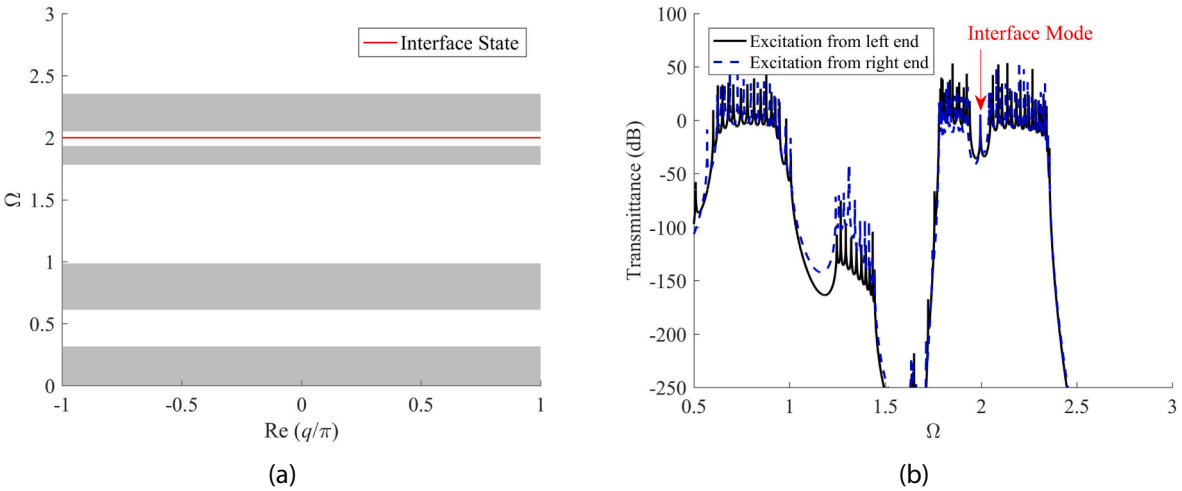

Fig. 15. (a) Band structure of the topological metamaterial, i.e., a supercell system that is constructed by assembling two types of metamaterial chains. Each metamaterial chain contains 10 unit cells. The red line indicates the appearance of the topological interface state in the band gap. (b) The transmittance spectrum of the corresponding topological metamaterial with a single supercell. The black solid line and the blue dashed line represent the results when the excitations are applied from the left and the right ends, respectively. The LHS *meta*-chain is tuned with the parameters of $\mu_{\mathrm{LHS}} = 0.6$, $\alpha_0 = 1$, $\gamma_{\mathrm{LHS}} = 1$, and $\beta_{\mathrm{LHS}} = 0.3$. The RHS *meta*-chain is tuned with the parameters of $\mu_{\mathrm{LHS}} = 0.486$, $\alpha_0 = 1$, $\gamma_{\mathrm{LHS}} = 1.035$, and $\beta_{\mathrm{LHS}} = -0.3$.

5.3. Discussions

The above numerical case studies have verified the existence of the interface states in the proposed metamaterial. Different from the topological phononic crystals/metamaterials proposed in [16,17,30], the interface state formation mechanism of the proposed metamaterial does not rely on reforming the host structure. Through this study, we have demonstrated that by manipulating only the design of local resonators, the polarization transition could be stimulated in metamaterials. The idea presented in this study represents a novel design methodology of topological metamaterials. The proof-of-concept is carried out based on a lumped parameter model, since its explicit analytical solutions can be easily derived to give in-depth insights into the underlying mechanism. However, this idea is not limited to the lumped parameter model. It can be extended and applied to engineer other practical topological systems based on realistic structures, such as beams and plates. As compared to the designs developed in the literature, the design philosophy presented in this work does not require any alternation of the host structure. For a practical engineering system, one can create topological interface states by attaching a series of carefully configured local resonators to the host structure without revising it. In this scenario, the methodology presented in this work provides alternate ways in designing metamaterials, which brings great convenience and value in practical applications.

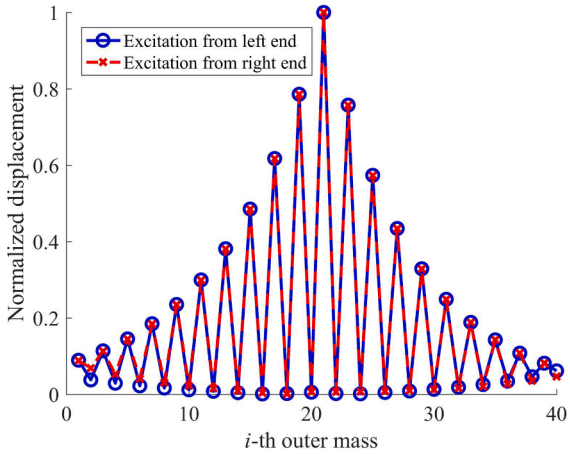

Fig. 16. Displacement distribution along the entire topological metamaterial chain. The *x*-axis denotes the number of the outer mass. The *y*-axis is the normalized displacement. The LHS *meta*-chain is tuned with the parameters of $\mu_{\mathrm{LHS}} = 0.6$, $\alpha_0 = 1$, $\gamma_{\mathrm{LHS}} = 1$, and $\beta_{\mathrm{LHS}} = 0.3$. The RHS *meta*-chain is tuned with the parameters of $\mu_{\mathrm{LHS}} = 0.486$, $\alpha_0 = 1$, $\gamma_{\mathrm{LHS}} = 1.035$, and $\beta_{\mathrm{LHS}} = -0.3$.

Prior to the concluding remarks, it is worth mentioning that the study presented in this work is limited to linear dynamics. It is well-known that nonlinear dynamics often produces more complicated and interesting phenomena, such as the amplitude-dependent behaviour, "stiffening/softening" effect, and multi-stable characteristics. Increasing interest has been attracted to investigate the influence of nonlinearities on topological metamaterials in recent years. For example, Pal *et al.* [32] revealed that by introducing nonlinearities at the interface of a topological PC lattice chain, the interface state exhibited an amplitude-dependent behaviour. Chaunsali *et al.* [33] constructed a PC lattice chain connected by alternating nonlinear springs. They disclosed that by just changing the excitation amplitude, the PC lattice chain self-induced a topological transition. Darabi *et al.* [34] periodically attached nonlinear resonators to a 2D PC lattice. The obtained topological system demonstrated an energy-dependency, i.e., under excitations of different energy levels, the interface state might be activated or inactivated. Other related works of nonlinear metamaterials can be found in [35–37]. As inspired by those results that nonlinearities can bring tunability and adaptivity, it is envisioned that by adopting the approaches in the above literature, there could be a potential opportunity to realize self-induced polarization transition and jumping phenomenon in the topological metamaterial proposed in this work.

6. Conclusions

In this study, we have developed a novel topological metamaterial with internally coupled resonators. The topological metamaterial is represented by a mass-spring model. Analytical solutions of the dispersion relation, bound evolution function, eigenvalues at all the bounds, etc. have been derived. Band inversion has been observed from the results of a bound evolution analysis. Conditions for polarization transition have been rigorously deduced. Three transition points were found in the proposed metamaterial, with each occurring in the first, second and third band gaps. When the coupling strength between the local resonators turns from positive to negative, the mode topologies of the bound states associated with the first and third band gaps can be converted. Unlike the first and third band gaps, the polarization transition in the second band gap activates when the coupling strength passes through a critical value around 0.514. In a word, changing the properties of the local resonators has been proven to open a chance for realizing polarization transition in the host structure (i.e., outer mass chain) of the metamaterial. By calculating the topological invariants, i.e., the Zak phases, of all the bands, the prediction about the occurrence of interface states in the proposed topological metamaterial has been ascertained. Using the transfer matrix method, we have examined the band structure and the transmittance spectrum of a supercell lattice of the proposed topological metamaterial. Numerical results have successfully validated the existence of interface states in all the three band gaps. The energy localization effect at the interface has been graphically illustrated through displacement distribution plots. In general, the design methodology presented in this work is of practical significance in transforming existing trivial structures into topological systems.

CRediT authorship contribution statement

Guobiao Hu: Conceptualization, Methodology, Software, Validation, Formal analysis, Investigation, Writing - original draft. **Chunbo Lan:** Formal analysis, Investigation, Writing - review & editing. **Lihua Tang:** Formal analysis, Investigation, Writing - review & editing. **Yaowen Yang:** Formal analysis, Investigation, Writing - review & editing, Supervision.

Declaration of Competing Interest

The authors declare that they have no known competing financial interests or personal relationships that could have appeared to

influence the work reported in this paper.

Appendix

$$C_6 = 2[(\alpha_1+\alpha_2+1)\mu+\beta+1]$$

$$C_4 = \left\{ \begin{array}{c} 2cos(q)\mu^2\alpha_1\alpha_2 - [2\alpha_1\alpha_2+2(\alpha_1+\alpha_2)+1]\mu^2 \\ -[(4\beta+4)(\alpha_1+\alpha_2)+4\beta+2]\mu-2\beta-1 \end{array} \right\}$$

$$C_2 = \mu\left[\begin{array}{c} -4\mu\alpha_1\alpha_2(\beta+1)cos(q)+(4\beta+2)(\alpha_1+\alpha_2)+2\beta \\ +[(4\beta+4)\alpha_1\alpha_2+(4\beta+2)(\alpha_1+\alpha_2)+2\beta]\mu \end{array} \right]$$

$$C_0 = 2\mu^2[cos(q)-1](2\beta\alpha_1+\beta+\alpha_1)\alpha_2$$

$$B_{11} = \frac{\Omega^4\mu^2-(2\beta_0\mu+2\mu\gamma)\Omega^2+2\beta_0\gamma+\gamma^2}{\Omega^4\mu^2-(2\beta_0\mu+2\mu\gamma)\Omega^2+\beta_0\gamma^2+2\beta_0\gamma+\gamma^2}$$

$$B_{12} = \frac{-\mu^2\Omega^6+(\mu^2\gamma+2\beta_0\mu+2\mu\gamma)\Omega^4-(2\beta_0\mu\gamma+\mu\gamma^2+2\beta_0\gamma+\gamma^2)\Omega^2}{\Omega^4\mu^2-(2\beta_0\mu+2\mu\gamma)\Omega^2+\beta_0\gamma^2+2\beta_0\gamma+\gamma^2}$$

$$B_{21} = \frac{\Omega^4\mu^2-(2\beta_0\mu+2\mu\gamma)\Omega^2+2\beta_0\gamma+\gamma^2}{\Omega^4\mu^2-(2\beta_0\mu+2\mu\gamma)\Omega^2+\beta_0\gamma^2+2\beta_0\gamma+\gamma^2}$$

$$B_{22} = \frac{\left[\begin{array}{c} -\mu^2\Omega^6+\left(\mu^2\gamma+2\beta_0\mu+\mu^2+2\mu\gamma\right)\Omega^4 \\ -\left(2\beta_0\mu\gamma+\mu\gamma^2+2\beta_0\mu+2\beta_0\gamma+2\mu\gamma+\gamma^2\right)\Omega^2+\beta_0\gamma^2+2\beta_0\gamma+\gamma^2 \end{array} \right]}{\Omega^4\mu^2-2(\beta_0\mu+2\mu\gamma)\Omega^2+\beta_0\gamma^2+2\beta_0\gamma+\gamma^2}$$

$$C_{11} = 1$$

$$C_{12} = \frac{-\mu^2\Omega^6+(\mu^2\gamma+2\beta_0\mu+2\mu\gamma)\Omega^4-(2\beta_0\mu\gamma+\mu\gamma^2+2\beta_0\gamma+\gamma^2)\Omega^2+\beta_0\gamma^2}{\Omega^4\mu^2-(2\beta_0\mu+2\mu\gamma)\Omega^2+2\beta_0\gamma+\gamma^2}$$

$$C_{21} = \alpha_0^{-1}$$

$$C_{22} = \frac{\left[\begin{array}{c} -\mu^2\Omega^6+\left(\alpha_0\mu^2+\mu^2\gamma+2\beta_0\mu+2\mu\gamma\right)\Omega^4 \\ -\left(2\alpha_0\beta_0\mu+2\alpha_0\mu\gamma+2\beta_0\mu\gamma+\mu\gamma^2+2\beta_0\gamma+\gamma^2\right)\Omega^2+2\alpha_0\beta_0\gamma+\alpha_0\gamma^2+\beta\gamma^2 \end{array} \right]}{\alpha_0\left(\Omega^4\mu^2-(2\beta_0\mu+2\mu\gamma)\Omega^2+2\beta_0\gamma+\gamma^2\right)}$$

$$D_{11} = 0$$

$$D_{12} = -\frac{\beta_0\gamma^2}{\Omega^4\mu^2-(2\beta_0\mu+2\mu\gamma)\Omega^2+2\beta_0\gamma+\gamma^2}$$

$$D_{21} = 0$$

$$D_{22} = -\frac{\beta_0\gamma^2}{\alpha_0\left(\Omega^4\mu^2-(2\beta_0\mu+2\mu\gamma)\Omega^2+2\beta_0\gamma+\gamma^2\right)}$$

References

[1] J. Page, A. Sukhovich, S. Yang, M. Cowan, F. Van Der Biest, A. Tourin, M. Fink, Z. Liu, C. Chan, P. Sheng, Phononic crystals, Phys. Status Solidi (B) 241 (15) (2004) 3454–3462.

[2] M. Lu, L. Feng, Y. Chen, Phononic crystals and acoustic metamaterials, Mater. Today 12 (12) (2009) 34–42.

[3] P.A. Deymier, Acoustic metamaterials and phononic crystals, Springer Science & Business Media, 2013.

[4] M.I. Hussein, M.J. Leamy, M. Ruzzene, Dynamics of phononic materials and structures: Historical origins, recent progress, and future outlook, Appl. Mech. Rev. 66 (4) (2014), 040802.

[5] A. Khelif, A. Adibi, Phononic Crystals: Fundamentals and Applications, Springer, New York, 2015.

[6] Y.-F. Wang, Y.-Z. Wang, B. Wu, W. Chen, Y.-S. Wang, Tunable and active phononic crystals and metamaterials, Appl. Mech. Rev. 72 (4) (2020), 040801.

[7] C. Brüne, A. Roth, H. Buhmann, E.M. Hankiewicz, L.W. Molenkamp, J. Maciejko, X.-L. Qi, S.-C. Zhang, Spin polarization of the quantum spin Hall edge states, Nat. Phys. 8 (6) (2012) 485–490.
[8] M. Tahir, A. Manchon, K. Sabeeh, U. Schwingenschlögl, Quantum spin/valley Hall effect and topological insulator phase transitions in silicene, Appl. Phys. Lett. 102 (16) (2013), 162412.
[9] R.K. Pal, M. Ruzzene, Edge waves in plates with resonators: an elastic analogue of the quantum valley Hall effect, New J. Phys. 19 (2) (2017), 025001.
[10] C.L. Kane, E.J. Mele, Z 2 topological order and the quantum spin Hall effect, Phys. Rev. Lett. 95 (14) (2005), 146802.
[11] J.E. Moore, The birth of topological insulators, Nature 464 (7286) (2010) 194–198.
[12] G. Ma, M. Xiao, C.T. Chan, Topological phases in acoustic and mechanical systems, Nat. Rev. Phys. 1 (4) (2019) 281–294.
[13] M.Z. Hasan, C.L. Kane, Colloquium: topological insulators, Rev. Mod. Phys. 82 (4) (2010) 3045.
[14] J. Yin, M. Ruzzene, J. Wen, D. Yu, L. Cai, L. Yue, Band transition and topological interface modes in 1D elastic phononic crystals, Sci. Rep. 8 (1) (2018) 1–10.
[15] M. Xiao, G. Ma, Z. Yang, P. Sheng, Z. Zhang, C.T. Chan, Geometric phase and band inversion in periodic acoustic systems, Nat. Phys. 11 (3) (2015) 240–244.
[16] D. Zhao, M. Xiao, C.W. Ling, C.T. Chan, K.H. Fung, Topological interface modes in local resonant acoustic systems, Phys. Rev. B 98 (1) (2018), 014110.
[17] L. Fan, Y. He, X. Zhao, X.-A. Chen, Subwavelength and broadband tunable topological interface state for flexural wave in one-dimensional locally resonant phononic crystal, J. Appl. Phys. 127 (23) (2020), 235106.
[18] A.B. Khanikaev, R. Fleury, S.H. Mousavi, A. Alu, Topologically robust sound propagation in an angular-momentum-biased graphene-like resonator lattice, Nat. Commun. 6 (1) (2015) 1–7.
[19] Z.-G. Chen, Y. Wu, Tunable topological phononic crystals, Phys. Rev. Appl 5 (5) (2016), 054021.
[20] M. Oudich, Y. Deng, M. Tao, Y. Jing, Space-time phononic crystals with anomalous topological edge states, Phys. Rev. Res. 1 (3) (2019), 033069.
[21] W.Z. Muhammad, C. Lim, Topological edge modeling and localization of protected interface modes in 1D phononic crystals for longitudinal and bending elastic waves, Int. J. Mech. Sci. 159 (2019) 359–372.
[22] Y. Jin, D. Torrent, B. Djafari-Rouhani, Robustness of conventional and topologically protected edge states in phononic crystal plates, Phys. Rev. B 98 (5) (2018), 054307.
[23] L. Fan, Y. He, X.-A. Chen, X. Zhao, Acoustic energy harvesting based on the topological interface mode of 1D phononic crystal tube, Appl. Phys Express 13 (1) (2019), 017004.
[24] H.-W. Dong, S.-D. Zhao, R. Zhu, Y.-S. Wang, L. Cheng, C. Zhang, Customizing acoustic dirac cones and topological insulators in square lattices by topology optimization, J. Sound Vib. 493 (2021), 115687.
[25] P. Wang, L. Lu, K. Bertoldi, Topological phononic crystals with one-way elastic edge waves, Phys. Rev. Lett. 115 (10) (2015), 104302.
[26] M. Atala, M. Aidelsburger, J.T. Barreiro, D. Abanin, T. Kitagawa, E. Demler, I. Bloch, Direct measurement of the Zak phase in topological Bloch bands, Nat. Phys. 9 (12) (2013) 795–800.
[27] P.A. Deymier, K. Runge, J. Vasseur, Geometric phase and topology of elastic oscillations and vibrations in model systems: Harmonic oscillator and superlattice, AIP Adv. 6 (12) (2016), 121801.
[28] D. Xiao, M.-C. Chang, Q. Niu, Berry phase effects on electronic properties, Rev. Mod. Phys. 82 (3) (2010) 1959.
[29] M. Wagner, F. Dangel, H. Cartarius, J. Main, G. Wunner, Numerical calculation of the complex berry phase in non-Hermitian systems, arXiv preprint arXiv: 1708.03230, 2017.
[30] A. Foehr, O.R. Bilal, S.D. Huber, C. Daraio, Spiral-based phononic plates: From wave beaming to topological insulators, Phys. Rev. Lett. 120 (20) (2018), 205501.
[31] G. Hu, L. Tang, J. Xu, C. Lan, R. Das, Metamaterial with Local Resonators Coupled by Negative Stiffness Springs for Enhanced Vibration Suppression, J. Appl. Mech. 86 (8) (2019), 081009.
[32] R.K. Pal, J. Vila, M. Leamy, M. Ruzzene, Amplitude-dependent topological edge states in nonlinear phononic lattices, Phys. Rev. E 97 (3) (2018), 032209.
[33] R. Chaunsali, G. Theocharis, Self-induced topological transition in phononic crystals by nonlinearity management, Physical Review B 100 (1) (2019), 014302.
[34] A. Darabi, M.J. Leamy, Tunable nonlinear topological insulator for acoustic waves, Phys. Rev. Appl 12 (4) (2019), 044030.
[35] X. Fang, J. Wen, B. Bonello, J. Yin, D. Yu, Wave propagation in one-dimensional nonlinear acoustic metamaterials, New J. Phys. 19 (5) (2017), 053007.
[36] R. Chaunsali, H. Xu, J. Yang, P.G. Kevrekidis, G. Theocharis, Stability of topological edge states under strong nonlinear effects, Phys. Rev. B 103 (2) (2021), 024106.
[37] X. Fang, J. Wen, B. Bonello, J. Yin, D. Yu, Ultra-low and ultra-broad-band nonlinear acoustic metamaterials, Nat. Commun. 8 (1) (2017) 1288.